Derivation of seawater $p\text{CO}_2$ from net community production identifies the South Atlantic Ocean as a CO_2 source

Formatted: Font: Italic

Daniel Ford[1,2], Gavin H. Tilstone[1], Jamie D. Shutler[2] and Vassilis Kitidis[1]

[1] Plymouth Marine Laboratory, Plymouth, UK
[2] College of Life and Environmental Sciences, University of Exeter, UK

Correspondence to: Daniel Ford (dfo@pml.ac.uk)

Abstract. A key step in assessing the global carbon budget is the determination of the partial pressure of CO_2 in seawater ($p\text{CO}_{2\ (\text{sw})}$). Spatially complete observational fields of $p\text{CO}_{2\ (\text{sw})}$ are routinely produced for regional and global ocean carbon budget assessments by extrapolating sparse *in situ* measurements of $p\text{CO}_{2\ (\text{sw})}$ using satellite observations. Within this~~ese~~ process~~schemes~~, satellite chlorophyll *a* (Chl *a*) is often used as a proxy for the biological drawdown or release of CO_2. Chl *a* does not however quantify carbon fixed through photosynthesis and then respired, which is determined by net community production (NCP).

Formatted: Font: Italic

Formatted: Font: Italic

Formatted: Font: Italic

In this study, $p\text{CO}_{2\ (\text{sw})}$ over the South Atlantic Ocean is estimated using a feed forward neural network (FNN) scheme and either satellite derived NCP, net primary production (NPP) or Chl *a* to compare which biological proxy is the most accurate. Estimates of $p\text{CO}_{2\ (\text{sw})}$ using NCP, NPP or Chl *a* were similar, but NCP was more accurate for the Amazon Plume and upwelling regions, which were not fully reproduced when using Chl *a* or NPP. A perturbation analysis assessed the potential maximum reduction in $p\text{CO}_{2\ (\text{sw})}$ uncertainties that could be achieved by ~~R~~reeducing the uncertainties in the satellite biological parameters ~~to estimate $p\text{CO}_{2\ (\text{sw})}$,~~ This illustrated further improvement ~~and greater differences~~ for NCP compared to NPP or Chl *a*. Using NCP to estimate $p\text{CO}_{2\ (\text{sw})}$ showed that the South Atlantic Ocean is a CO_2 source, whereas if no biological parameters are used in the FNN (following existing annual carbon assessments), this region becomes a sink for CO_2. These results highlight that using NCP improved the accuracy of estimating $p\text{CO}_{2\ (\text{sw})}$, and changes the South Atlantic Ocean from a CO_2 sink to a source. Reducing the uncertainties in NCP derived from satellite parameters will further improve our ability to quantify the global ocean CO_2 sink.

Formatted: Font: Italic

Formatted: Font: Italic

Formatted: Font: Italic

Formatted: Font: Italic

Formatted: Font: Italic

1. Introduction

Since the industrial revolution, anthropogenic CO_2 emissions have resulted in an increase in atmospheric CO_2 concentrations (Friedlingstein et al., 2020; IPCC, 2013). By acting as a sink for CO_2, the oceans have buffered the increase in anthropogenic atmospheric CO_2, without which the atmospheric concentration would be 42-44 % higher (DeVries, 2014). The long-term absorption of CO_2 by the oceans is altering the marine carbonate chemistry of the ocean, resulting in a lowering of pH,~~;~~ a process known as ocean acidification (Raven et al., 2005). Observational fields of the partial pressure of CO_2 in seawater ($p\mathrm{CO}_{2\,\mathrm{(sw)}}$) are one of the key datasets needed to routinely assess the strength of the oceanic CO_2 sink (Friedlingstein et al., 2020; Landschützer et al., 2014, 2020; Rödenbeck et al., 2015; Watson et al., 2020b). These methods are reliant on the extrapolation of sparse *in situ* observations of $p\mathrm{CO}_{2\,\mathrm{(sw)}}$ using satellite observations of parameters which account for the variability of, and the controls on, $p\mathrm{CO}_{2\,\mathrm{(sw)}}$ (Shutler et al., 2020). These parameters include sea surface temperature (SST; e.g. Landschützer et al., 2013; Stephens et al., 1995), salinity and chlorophyll *a* (Chl *a*) (Rödenbeck et al., 2015). SST and salinity control $p\mathrm{CO}_{2\,\mathrm{(sw)}}$ by changing the solubility of CO_2 in seawater (Weiss, 1974), whilst biological processes such as photosynthesis and respiration contribute by modulating its concentration.

Chl *a* is routinely used as a proxy for this biological activity (Rödenbeck et al., 2015), but it does not distinguish between carbon fixation through photosynthesis and the carbon respired by the plankton community. Net primary production (the net carbon fixation rate; NPP) is determined by the standing stock of phytoplankton, for which the Chl *a* concentration is used as a proxy, and modified by the photosynthetic rate and the available light in the water column (Behrenfeld et al., 2016). Photosynthetic rates are, in turn, modified by ambient nutrient and temperature conditions (Behrenfeld and Falkowski, 1997; Marañón et al., 2003). Elevated Chl *a* does not always equate to elevated NPP (Poulton et al., 2006), and for the same Chl *a* concentrations, NPP can vary depending on the health and metabolic state of the plankton community. All of these controls are captured by the net community production (NCP), which is the metabolic balance of the plankton community resulting from the carbon fixed through photosynthesis and that lost through respiration. When NCP is positive, the plankton community is autotrophic which implies that there is a drawdown of CO_2 from seawater (since the plankton reduce the CO_2 in the water column).~~, and~~ Where NCP~~when it~~ is negative the community is heterotrophic implying a release of CO_2 into the ocean (as the plankton produce or release CO_2) which can then be released into the atmosphere (Jiang et al., 2019; Schloss et al., 2007). Using NCP to estimate $p\mathrm{CO}_{2\,\mathrm{(sw)}}$ compared to Chl *a* should ~~therefore~~ theoretically lead to an improvement in the derivation of $p\mathrm{CO}_{2\,\mathrm{(sw)}}$.

Many studies have used satellite Chl *a* to estimate $p\mathrm{CO}_{2\,\mathrm{(sw)}}$ at both regional (Benallal et al., 2017; Chierici et al., 2012; Moussa et al., 2016), and global scales (Landschützer et al., 2014; Liu and Xie, 2017). Chierici et al. (2012) attempted to use satellite NPP to estimate $p\mathrm{CO}_{2\,\mathrm{(sw)}}$ in the southern Pacific Ocean, but there was no significant improvement over using satellite Chl *a*. This is not surprising as NPP captures more of the biological signal, but still lacks any inclusion of respiration which results in the release of CO_2 into the water column. To our knowledge the use of satellite NCP to estimate $p\mathrm{CO}_{2\,\mathrm{(sw)}}$ has not been attempted before and could be a means of improving estimates of $p\mathrm{CO}_{2\,\mathrm{(sw)}}$ as long as satellite NCP observations are accurate (Ford et al., 2021b; Tilstone et al., 2015a). These satellite measurements may improve the estimation of $p\mathrm{CO}_{2\,\mathrm{(sw)}}$ as NCP includes the full biological control on $p\mathrm{CO}_{2\,\mathrm{(sw)}}$.~~, which could be~~This is particularly important in regions ~~regions of sparse~~where *in situ* $p\mathrm{CO}_{2\,\mathrm{(sw)}}$ observations are sparse and where interpolation and neural network techniques are therefore likely to struggle (Watson et al., 2020b).

The South Atlantic Ocean is under sampled with limited $p\mathrm{CO}_{2\,\mathrm{(sw)}}$ observations (e.g. Fay and McKinley, 2013; Watson et al., 2020b). The region is varied and dynamic as it includes the seasonal Equatorial upwelling, high biological activity on the

Formatted: Font: Italic
Formatted: Font: Italic
Formatted: Font: Italic
Formatted: Font: Italic
Formatted: Font: Italic
Formatted: Font: Italic
Formatted: Font: Italic
Formatted: Font: Italic
Formatted: Font: Italic
Formatted: Font: Italic
Formatted: Font: Italic
Formatted: Font: Italic
Formatted: Font: Italic
Formatted: Font: Italic
Formatted: Font: Italic
Field Code Changed

south-western (Dogliotti et al., 2014) and south-eastern shelves (Lamont et al., 2014), as well as the propagation of the Amazon Plume into the western Equatorial Atlantic (Ibánhez et al., 2015). This in conjunction with a comprehensive database of satellite observation-based data with associated uncertainties (Ford et al., 2021b) provides the potential to identify the improvement to $p\text{CO}_{2\text{ (sw)}}$ estimates that could be made from using NCP.

The objective of this paper is ~~therefore~~ to compare the estimation of $p\text{CO}_{2\text{ (sw)}}$ using either NCP, NPP or Chl *a* to determine which biological descriptor is the most accurate. A 16 year time series of $p\text{CO}_{2\text{ (sw)}}$ was generated for the South Atlantic Ocean using satellite NCP, NPP or Chl *a*, as the biological input, alongside a ~~baseline~~ two approaches with no biological parameters as input. Regional differences in the generated $p\text{CO}_{2\text{ (sw)}}$ fields are assessed. The seasonal and interannual variability in $p\text{CO}_{2\text{ (sw)}}$ estimated from NCP, NPP, Chl *a* and the ~~baseline~~ approaches with no biological parameters were also compared. A perturbation analysis was conducted to evaluate the potential reduction in the uncertainty in the $p\text{CO}_{2\text{ (sw)}}$ fields when estimated from NCP, NPP or Chl *a*. This is discussed in the context of reducing uncertainties in these input variables for future improvements in producing spatially complete fields of $p\text{CO}_{2\text{ (sw)}}$, and the effect on estimates of the oceanic carbon sink.

Formatted: Font: Not Italic

Formatted: Font: Not Italic

Field Code Changed

Formatted: Font: Not Italic

Formatted: Font: Not Italic

Formatted: Font: Italic

Formatted: Font: Italic

Formatted: Font: Italic

Formatted: Font: Italic

Formatted: Font: Italic

Formatted: Font: Italic

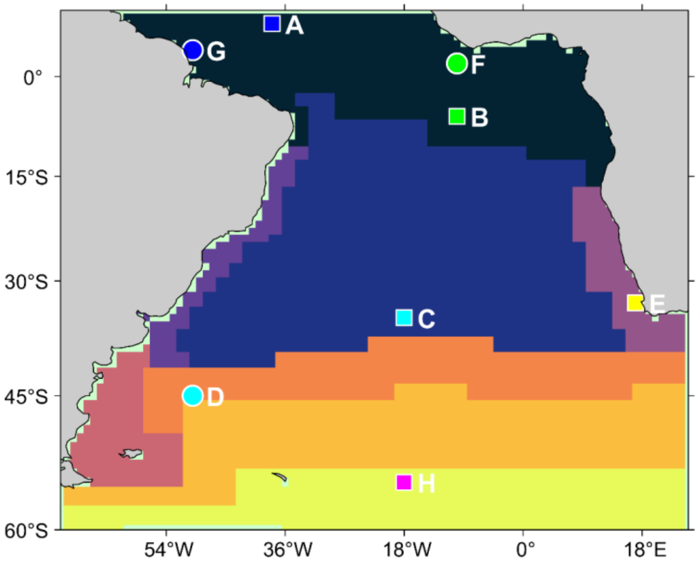

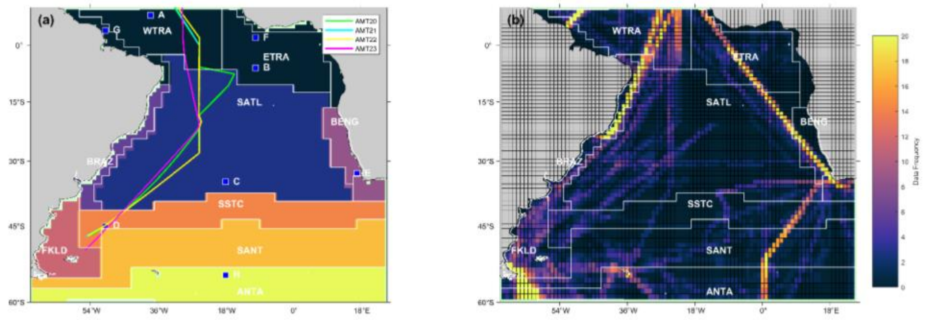

Fig. 1: (a) Map of the 8 static biogeochemical provinces in the South Atlantic Ocean, following Longhurst et al. (1995) and Longhurst (1998). Markers and letters indicate the locations of timeseries extracted from~~in~~ Fig. 3. The four Atlantic Meridional Transect (AMT) cruise tracks are also overlaid (b) Map showing the spatial distribution of the SOCATv2020 dataset used, where the data frequency is the number of available months of data within each 1° pixel. The province areas acronyms are: WTRA is Western Tropical Atlantic; ETRA is Eastern Equatorial Atlantic; SATL is South Atlantic Gyre; BRAZ is Brazilian current coastal; BENG is Benguela Current coastal upwelling; FKLD is Southwest Atlantic shelves; SSTC is South Subtropical Convergence; SANT is Sub Antarctic and ANTA is Antarctic.

Field Code Changed

Formatted: Font: Bold

Formatted: Font: Bold

Field Code Changed

2. Methods

2.1. Surface Ocean Carbon Atlas (SOCAT) $p\mathrm{CO_{2\,(sw)}}$ and atmospheric $\mathrm{CO_2}$

SOCATv2020 (Bakker et al., 2016; Pfeil et al., 2013) individual fugacity of $\mathrm{CO_2}$ in seawater ($f\mathrm{CO_{2\,(sw)}}$) observations were downloaded from https://www.socat.info/index.php/data-access/. Data were extracted from 2002 to 2018 for the South Atlantic Ocean (10º N-60º S, 25º E–80º W; Fig. 1b). The individual cruise observations were collected from different depths, and are not representative of the $f\mathrm{CO_{2\,(sw)}}$ in the top ~100 µm of the ocean, where gas exchange occurs (Goddijn-Murphy et al., 2015; Woolf et al., 2016). Therefore, the SOCAT observations were re-analysed to a standard temperature dataset and depth (Reynolds et al., 2002) that is considered representative of the bottom of the mass boundary layer (Woolf et al., 2016). This was achieved using the 'fe_reanalyse_socat' utility in the open source FluxEngine toolbox (Holding et al., 2019; Shutler et al., 2016), which follows the methodology described in Goddijn-Murphy et al. (2015). The reanalysed $f\mathrm{CO_{2\,(sw)}}$ observations were converted to $p\mathrm{CO_{2\,(sw)}}$, and gridded onto 1º monthly grids following SOCAT protocols (Sabine et al., 2013). The uncertainties in the *in situ* data were taken as the standard deviation of the observations in each grid cell, or where a single observation exists were set as 5 µatm following Bakker et al. (2016).

SOCATv2020 Flag E $f\mathrm{CO_{2\,(sw)}}$ observations were also downloaded from https://www.socat.info/index.php/data-access/. These data represent observations collected using non-standard techniques, with accuracies < 10 µatm, generally associated with autonomous buoy and drifter measurements. These data were processed identically to the main SOCATv2020 $f\mathrm{CO_{2\,(sw)}}$ and converted to $p\mathrm{CO_{2\,(sw)}}$.

Monthly 1º grids of atmospheric $p\mathrm{CO_2}$ ($p\mathrm{CO_{2\,(atm)}}$) were extracted from v5.5 of the global estimates of $p\mathrm{CO_{2\,(sw)}}$ dataset (Landschützer et al., 2016, 2017). $p\mathrm{CO_{2\,(atm)}}$ was estimated using the dry mixing ratio of $\mathrm{CO_2}$ from the NOAA-ESRL marine boundary layer reference (https://www.esrl.noaa.gov/gmd/ccgg/mbl/), Optimum Interpolated SST (Reynolds et al., 2002) and sea level pressure following Dickson et al. (2007).

2.2. Moderate Resolution Spectroradiometer on Aqua (MODIS-A) satellite observations

4 km resolution monthly mean Chl *a* were calculated from MODIS-A Level 1 granules, retrieved from National Aeronautics and Space Administration (NASA) Ocean Colour website (https://oceancolor.gsfc.nasa.gov/) using SeaDAS v7.5, and applying the standard OC3-CI Chl *a* algorithm (https://oceancolor.gsfc.nasa.gov/atbd/chlor_a/). In addition, monthly mean MODIS-A SST and photosynthetically active radiation (PAR) were also downloaded from the NASA Ocean Colour website. Mean monthly NPP were generated from MODIS-A Chl *a*, SST and PAR using the Wavelength Resolving Model (Morel, 1991) with the look up table described in Smyth et al. (2005). Coincident mean monthly NCP using the algorithm NCP-D described in Tilstone et al. (2015a) were generated using the MODIS-A NPP and SST data. Further details of the satellite algorithms are given in O'Reilly et al. (1998; 2019), Hu et al. (2012) for Chl *a*, Smyth et al. (2005), Tilstone et al. (2005, 2009) for NPP and Tilstone et al. (2015a) for NCP. These satellite algorithms were the most accurate for the South Atlantic

Formatted: Font: Italic

Formatted: Font: Italic

Formatted: Font: Italic

Formatted: Font: Italic

Formatted: Font: Italic

Formatted: Font: Italic

Formatted: Not Superscript/ Subscript

Formatted: Font: Italic

Formatted: Font: Italic

Formatted: Font: Italic

Formatted: Font: Italic

Ocean in an algorithm inter-comparison which accounting for the uncertainties in both *in situ*, model and input data (Ford et al., 2021b). All monthly mean data were generated between July 2002 and December 2018 and were re-gridded onto the same 1º grid as the *p*$CO_{2\ (sw)}$ observations. The assessed uncertainties from the literature for each of the input parameters used are given in Table 1.

Formatted: Font: Italic

Formatted: Font: Italic

Table 1: Uncertainties in the input parameters of the Feed Forward Neural Network used in Monte Carlo uncertainty propagation and perturbation analysis.

Parameter	Algorithm Uncertainty	Reference
Chlorophyll *a*	0.15 $\log_{10}(\mathrm{mg\ m^{-3}})$	Ford~~,~~ et al. (2021b)
Net Primary Production	0.20 $\log_{10}(\mathrm{mg\ C\ m^{-2}\ d^{-1}})$	Ford~~,~~ et al. (2021b)
Net Community Production	45 mmol $\mathrm{O_2\ m^{-2}\ d^{-1}}$	Ford~~,~~ et al. (2021b)
SST	0.41 ºC	Ford~~,~~ et al. (2021b)
$p\mathrm{CO}_{2\,\mathrm{(atm)}}$	1 µatm	~~(~~Takahashi et al.~~,~~ (2009)

Formatted: Font: Italic

2.3. Feed forward neural network scheme

The South Atlantic Ocean was partitioned into 8 biogeochemical provinces (Fig. 1a), following Longhurst et al. (1995) and Longhurst (1998). The $p\mathrm{CO}_{2\,\mathrm{(sw)}}$ observations in the eastern Equatorial Atlantic were sparse, and therefore the Equatorial region was merged into 1 province. In each province the available monthly $p\mathrm{CO}_{2\,\mathrm{(sw)}}$ observations were matched to temporally and spatially coincident $p\mathrm{CO}_{2\,\mathrm{(atm)}}$, MODIS-A, NCP and SST, to provide training data for the feed forward neural network (FNN). Observations in coastal regions (< 200 m water depth) were removed from the analysis, due to the increased uncertainty in ocean colour observations in these areas (e.g. Lavender et al., 2004). Due to constraints on the coverage of ocean colour data, no data were available in austral winter below ~50º S.

Formatted: Font: Italic

Formatted: Font: Italic

Formatted: Font: Italic

The coincident observations in each province were randomly split into 3 datasets: 1.) A training dataset (50 % of the observations) used to train the FNNs; 2.) A validation dataset (30 % of the observations) used to assess the performance of the FNN and to prevent the networks from overfitting; 3.) An independent test dataset (20 % of the observations) to assess the final performance of the FNN, with observations that are independent of the network training. The optimal split (r_{opt}) method of Amari et al. (1997) was used to partition the input data into these three sets, as follows:

$$r_{opt} = 1 - \frac{1}{\sqrt{2m}} \qquad (1)$$

where m is number of input parameters. For our three input parameters, ~~a~~an optimal split of 60 % training data to 40 % validation data~~sets~~ would occur, where we removed 10 % from each dataset to provide a further independent test dataset. A pre-training step was used to determine the optimum number of hidden neurons in the FNN (Benallal et al., 2017; Landschützer et al., 2013; Moussa et al., 2016), to provide the best fit for the observations, whilst preventing over fitting (Demuth et al., 2008).

The FNNs consist of 1 hidden layer with between 2 and 30 nodes depending on the pre-training step and 1 output layer. ~~The FNN~~The networks were~~as~~ trained using the optimum number of hidden neurons, in an iterative process until the Root Mean Square Difference (RMSD) remained unchanged for 6 iterations. The best performing FNN, with the lowest RMSD was then used to estimate $p\mathrm{CO}_{2\,\mathrm{(sw)}}$. The uncertainties in the input parameters were propagated through the FNN, using a Monte Carlo

Formatted: Font: Italic

uncertainty propagation, where 1000 calculations were made perturbing the input parameters, using random noise for their uncertainty (Table 1). The output from the 8 province FNNs were then combined and weighted statistics, which account for both the satellite and *in situ* uncertainty, were used to assess the overall performance of the FNN (as used within Ford et al., 2021b). The combined 8 FNNs approach will hereafter be referred to as SA-FNN.

The approach to training the FNNs was repeated replacing NCP with Chl *a* or NPP sequentially, to determine if there was an improvement by using NCP. Chl *a* and NPP estimates were log$_{10}$ transformed before input into the FNN, due to their respective uncertainties being determined in log$_{10}$ space (Table 2). A baseline SA-FNN with no biological parameters as input was trained using pCO$_{2\ \text{(atm)}}$ and~~,~~ MODIS-A SST (SA-FNN$_{\text{NO-BIO-1}}$). A second SA-FNN with no biological parameters (SA-FNN$_{\text{NO-BIO-2}}$) was trained with the addition of~~, alongside~~ sea surface salinity and mixed layer depth from the Copernicus Marine Environment Modelling Service (https://resources.marine.copernicus.eu/) global ocean physics reanalysis product (GLORYS12V1). This parameter combination (pCO$_{2\ \text{(atm)}}$, SST, salinity and mixed layer depth) has recently been included within a neural network scheme to estimate global fields of pCO$_{2\ \text{(sw)}}$ (Watson et al., 2020b).

Following these methods, a monthly mean time-series of pCO$_{2\ \text{(sw)}}$ was generated in the South Atlantic Ocean, applying the SA-FNN approach using NCP (SA-FNN$_{\text{NCP}}$), NPP (SA-FNN$_{\text{NPP}}$), Chl *a* (SA-FNN$_{\text{CHLA}}$) or no biological parameters (SA-FNN$_{\text{NO-BIO-1}}$ and SA-FNN$_{\text{NO-BIO-2}}$). The pCO$_{2\ \text{(sw)}}$ fields were spatially averaged using a 3×3 pixel filter, but were not averaged temporally as in previous studies (Landschützer et al., 2014, 2016) because averaging temporally could mask features that occur within single months of the year. The uncertainties in the input parameters (Table 1) were propagated through the neural network on a per pixel basis, and combined in quadrature with the RMSD of the test dataset, to produce a combined uncertainty budget for each pixel, assuming all sources of uncertainty are independent and uncorrelated (BIPM, 2008; Taylor, 1997).

2.4. Atlantic Meridional Transect *in situ* data

To assess the accuracy of the SA-FNN, coincident *in situ* measurements of NCP, NPP, Chl *a*, SST, pCO$_{2\ \text{(atm)}}$ and pCO$_{2\ \text{(sw)}}$, with uncertainties, were provided by Atlantic Meridional Transects 20, 21, 22 and 23 in 2010, 2011, 2012 and 2013, respectively. All the Atlantic Meridional Transect data described in this section can be obtained from the British Oceanographic Data Centre (https://www.bodc.ac.uk/). Chl *a* was ~~estimated~~ computed following the methods of Brewin et al. (2016), using underway continuous spectrophotometric measurements, and uncertainties were estimated as ~0.06 log$_{10}$(mg m^{-3}) (Ford et al., 2021b). ^{14}C based NPP measurements were made based on dawn to dusk simulated *in situ* incubations, following the methods given in Tilstone et al. (2017), at 56 stations with a per station uncertainty. Uncertainties ranged between 8 and 213 mg C m^{-2} d^{-1} and were on average 53 mg C m^{-2} d^{-1}. NCP was estimated using *in vitro* changes in dissolved O$_2$, following the methods of Gist et al. (2009) and Tilstone et al. (2015a) at 51 stations with a per station uncertainty calculated. Uncertainties ranged between 5 and 25 mmol O$_2$ m^{-2} d^{-1} and were on average 14 mmol O$_2$ m^{-2} d^{-1}.

Underway measurements of pCO$_{2\ \text{(sw)}}$ and pCO$_{2\ \text{(atm)}}$ were performed continuously, following the methods of Kitidis et al. (2017). SST was continuously measured alongside all observations (SeaBird SBE45), with a factory calibrated uncertainty of

Formatted: Font: Italic

Formatted: Subscript

Formatted: Subscript

Formatted: Font: Italic

Formatted: Font: Italic

Formatted: Font: Italic

Formatted: Font: Italic

Formatted: Font: Italic

Formatted: Font: Italic

Formatted: Font: Italic

Formatted: Font: Italic

Formatted: Font: Italic

±0.01 °C. The mean of underway $p\mathrm{CO}_{2\ (\mathrm{sw})}$, $p\mathrm{CO}_{2\ (\mathrm{atm})}$, SST and Chl *a* were taken ±20 minutes around each station where NCP and NPP were measured. These $p\mathrm{CO}_{2\ (\mathrm{sw})}$ observations (N≈200) were removed from the SOCATv2020 dataset so that the Atlantic Meridional Transect data remained independent from the training and validation datasets.

2.5. Perturbation analysis

Following the approach of Saba et al. (2011), a perturbation analysis was conducted, to evaluate the potential reduction in SA-FNN $p\mathrm{CO}_{2\ (\mathrm{sw})}$ RMSD that could be attributed to the input parameters. The analysis indicates the maximum reduction in RMSD that could be achieved if uncertainties in the input parameters were reduced to ~0. Each of the input parameters; NCP, SST and $p\mathrm{CO}_{2\ (\mathrm{atm})}$ can have three possible values for each *in situ* $p\mathrm{CO}_{2\ (\mathrm{sw})}$ ~~estimate~~ observation (original value, original ± uncertainty; Table 1), enabling 27 perturbations of the input data as input to the SA-FNN. ~~RMSD and bias were used to assess the performance of SA-FNN under different scenarios.~~ For each *in situ* $p\mathrm{CO}_{2\ (\mathrm{sw})}$ observation, the 27 perturbations of SA-FNN $p\mathrm{CO}_{2\ (\mathrm{sw})}$ were examined, and the perturbation that produced the lowest RMSD and bias combination was selected. The RMSD and bias were calculated between all the *in situ* $p\mathrm{CO}_{2\ (\mathrm{sw})}$ and the selected perturbations. The percentage difference between this RMSD and the original RMSD when training the SA-FNN was calculated to indicate the maximum achievable reduction. This approach was conducted for~~ in~~ two scenarios~~ was selected~~; (1) uncertainty in individual input parameters (NCP, SST and $p\mathrm{CO}_{2\ (\mathrm{atm})}$) and (2) uncertainty in all input parameters together. The approach was conducted on all three training datasets, and on the Atlantic Meridional Transect *in situ* data. The analysis was repeated sequentially replacing NCP with Chl *a* and NPP, to determine if there was a greater maximum reduction in RMSD using NCP. The analysis was also conducted allowing for a 10 % reduction in input parameter uncertainties, to indicate the short-term reduction in $p\mathrm{CO}_{2\ (\mathrm{sw})}$ RMSD that could be achieved by reducing the input parameter uncertainties.

2.6. Comparison of the SA-FNN$_{\mathrm{NCP}}$ with the SA-FNN$_{\mathrm{NO\text{-}BIO}}$, SA-FNN$_{\mathrm{CHLA}}$, SA-FNN$_{\mathrm{NPP}}$ and 'state of the art' data for the South Atlantic

The most comprehensive $p\mathrm{CO}_{2\ (\mathrm{sw})}$ fields to date are from Watson et al. (2020b, 2020a). The 'standard method' $p\mathrm{CO}_{2\ (\mathrm{sw})}$ fields within the Watson et al. (2020b, 2020a) data were produced by extrapolating the *in situ* reanalysed SOCATv2019 $p\mathrm{CO}_{2\ (\mathrm{sw})}$ observations using a self-organising map feed forward neural network approach (Landschützer et al., 2016), and will be referred to as 'W2020'. A time-series was extracted from the W2020 data, coincident with~~to~~ SA-FNN$_{\mathrm{NCP}}$, SA-FNN$_{\mathrm{NPP}}$, SA-FNN$_{\mathrm{CHLA}}$ and the two SA-FNN$_{\mathrm{NO\text{-}BIO}}$ variants. For the six~~five~~ methods, a monthly climatology referenced to the year 2010 was computed, assuming an atmospheric $\mathrm{CO_2}$ increase of 1.5 µatm yr^{-1} (Takahashi et al., 2009; Zeng et al., 2014). The climatology should be insensitive to the ~~chosen~~ assumed rise in atmospheric $\mathrm{CO_2}$ ~~rise~~ due to the reference year being central to the time series. The standard deviation of this climatology was also computed on a per pixel basis.

The stations (Fig. 1) are representative of locations from previous literature that analysed the variability of *in situ* $p\mathrm{CO}_{2\ (\mathrm{sw})}$ in the South Atlantic Ocean. For each station~~ in Fig. 1~~, the monthly climatology of $p\mathrm{CO}_{2\ (\mathrm{sw})}$, representing the average seasonal cycle of $p\mathrm{CO}_{2\ (\mathrm{sw})}$, and the standard deviation of the climatology, as an indication of the interannual variability, were

Formatted: Font: Italic
Formatted: Font: Italic
Formatted: Font: Italic
Formatted: Font: Italic
Formatted: Font: Italic
Formatted: Font: Italic
Formatted: Font: Italic
Formatted: Font: Italic
Formatted: Font: Italic
Formatted: Font: Italic
Formatted: Font: Italic
Formatted: Font: Italic
Formatted: Font: Italic
Formatted: Font: Italic
Formatted: Font: Italic
Formatted: Font: Italic
Formatted: Font: Italic

extracted from the six~~five~~ approaches. The *p*$CO_{2\,(sw)}$ value for each station was the statistical mean of the four nearest data points weighted by their respective proximity to the station coordinate. *In situ p*$CO_{2\,(sw)}$ observations from the SOCATv2020 Flag E dataset were also extracted for stations A and B (Fig. 1a), and a climatology was generated. These observations represent data from the Prediction and Research Moored Array in the Atlantic (PIRATA) buoys at these locations (Bourlès et al., 2008).

The station climatologies for the SA-FNN$_{\text{NO-BIO-1}}$, SA-FNN$_{\text{NO-BIO-2}}$, W2020, SA-FNN$_{\text{CHLA}}$, and SA-FNN$_{\text{NPP}}$ were compared to the SA-FNN$_{\text{NCP}}$, by testing for significant differences in the seasonal cycle and annual *p*$CO_{2\,(sw)}$ (offset). The seasonal cycles (seasonality) were compared using a non-parametric Spearman's correlation and deemed statistically different where the correlation was not significant ($\alpha < 0.05$). A non-parametric Kruskal-Wallis was used to test for~~tested for~~ significant ($\alpha < 0.05$) differences in the annual *p*$CO_{2\,(sw)}$, indicating an offset between the two tested climatologies. The Southern Ocean station (station H) was excluded from the statistical analysis due to missing data in the SA-FNN.

2.7. Estimation of the bulk CO$_2$ flux

The flux of CO_2 (F) between the atmosphere and ocean (air-sea) can be expressed in a bulk parameterisation as:

$$F = k\,(\alpha_W\, pCO_{2\,(sw)} - \alpha_s\, pCO_{2\,(atm)}) \qquad (2)$$

Where k is the gas transfer velocity, and α_w and α_s are the solubility of CO_2 at the base and top of the mass boundary layer at the sea surface respectively (Woolf et al., 2016). k was estimated from ERA5 monthly reanalysis wind speed (downloaded from the Copernicus Climate Data Store; https://cds.climate.copernicus.eu/) following the parameterisation of Nightingale et al. (2000). The parameter α_w was estimated as a function of SST and sea surface salinity (Weiss, 1974) using the monthly Optimum Interpolated SST (Reynolds et al., 2002) and sea surface salinity from the Copernicus Marine Environment Modelling Service global ocean physics reanalysis product (GLORYS12V1). The α_s parameter was estimated using the same temperature and salinity datasets but included a gradient from the base to the top of mass boundary layer of -0.17 K (Donlon et al., 1999) and +0.1 salinity units (Woolf et al., 2016). *p*$CO_{2\,(atm)}$ was estimated using the dry mixing ratio of CO_2 from the NOAA-ESRL marine boundary layer reference, Optimum Interpolated SST (Reynolds et al., 2002) applying a cool skin bias (0.17K; Donlon et al., 1999) and sea level pressure following Dickson et al. (2007). Spatially and temporally complete *p*$CO_{2\,(sw)}$ fields, which are representative of *p*$CO_{2\,(sw)}$ at the base of the mass boundary layer, were extracted from the SA-FNN$_{\text{NCP}}$, SA-FNN$_{\text{NPP}}$, SA-FNN$_{\text{CHLA}}$, SA-FNN$_{\text{NO-BIO-1}}$, SA-FNN$_{\text{NO-BIO-2}}$ and W2020.

The monthly CO_2 flux was calculated using the open source FluxEngine toolbox (Holding et al., 2019; Shutler et al., 2016) between 2003 and 2018 for the six~~five~~ *p*$CO_{2\,(sw)}$ inputs, using the 'rapid transport' approximation (described in Woolf et al., 2016). The net annual flux was determined for the South Atlantic Ocean (10° N-44° S; 25° E-70° W) using the 'fe_calc_budgets.py' utility within FluxEngine with the supplied area and land percentage masks. The mean net annual flux was calculated as the mean of the 15 year net annual fluxes. Positive net fluxes indicate a net source to the atmosphere, and negative net fluxes a sink.

Formatted: Font: Italic

Formatted: Font: Italic

Formatted: Font: Italic

Formatted: Font: Italic

Formatted: Font: Italic

Formatted: Font: Italic

Formatted: Font: Italic

Table 2: The percentage reduction in $p\mathrm{CO}_{2\,(sw)}$ RMSD by reducing NCP, ~~net primary production~~NPP and ~~chlorophyll *a*~~*Chl a* uncertainties to ~0 as described in Section 2.5. The full results can be found in Appendix Table A1.

Formatted: Font: Italic

Parameter	Training	Validation	Independent Test	AMT *in situ*
NCP	32 %	40 %	36 %	25 %
~~Net Primary Production~~NPP	31 %	37 %	36 %	13 %
~~Chlorophyll *a*~~Chl *a*	17 %	21 %	20 %	7 %

Formatted: Font: Italic

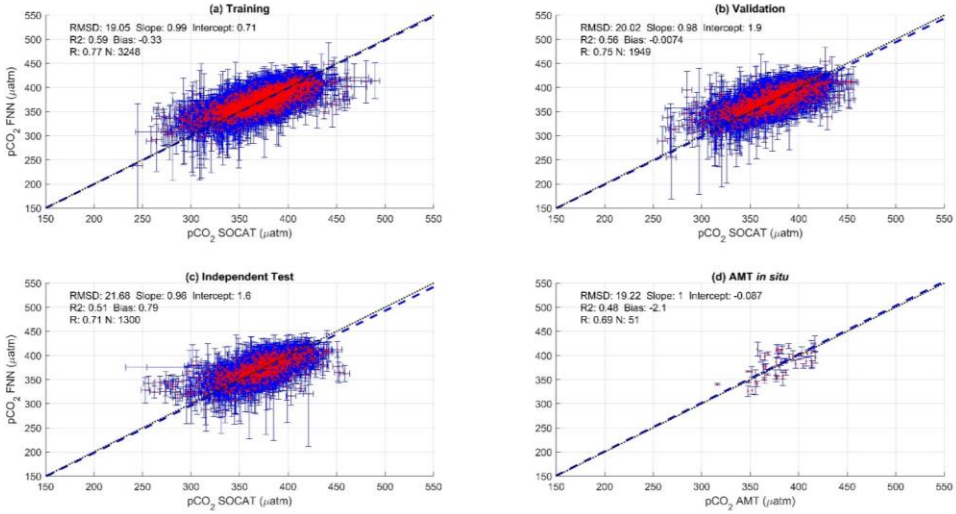

Fig. 2: Scatter plots showing the combined performance of the 8 feed forward neural networks trained using NCP for each biogeochemical province (Fig. 1) using 4 separate training and validation datasets; (a) Training, (b) Validation, (c) Independent Test and (d) Atlantic Meridional Transect (AMT) in situ. –The data points are highlighted in red to distinguish them from the error bars in blue. The blue dashed line is the Type II regression and the black dashed line is the 1:1 line. Horizontal error bars indicate the uncertainty of the SOCATv2020 $p\mathrm{CO}_{2\,(sw)}$. Vertical error bars indicate the uncertainty attributed to the input parameter uncertainty propagated through the feed forward neural networks. The statistics within each plot are; Root Mean

Formatted: Font: Italic

Square Difference (RMSD), Slope and Intercept of the Type II regression, Coefficient of Determination (R2), Pearson's Correlation Coefficient (R), Bias and number of samples (N).

Table 3: The percentage reduction in $p\mathrm{CO}_{2\ (\mathrm{sw})}$ RMSD by reducing NCP, net primary production and chlorophyll a uncertainties by 10 % as described in Section 2.5.

Parameter	Training	Validation	Independent Test	AMT *in situ*
NCP	7 %	8 %	8 %	3 %
~~Net Primary Production~~NPP	5 %	6 %	5 %	1.5 %
Chl~~orophyll~~ *a*	2 %	2 %	2 %	0.5 %

3. Results

3.1. SA-FNN performance and perturbation analysis

The performance of the SA-FNN trained using $p\mathrm{CO}_{2\ (\mathrm{atm})}$, SST and NCP for the three training datasets is given in Fig. 2. The SA-FNN$_{\mathrm{NCP}}$ had an accuracy (RMSD) of 21.68~~7~~ µatm and a precision (bias) of 0.87 µatm, which was determined with the independent test data (N = 1300). Training the SA-FNN using Chl *a* or NPP instead of NCP, resulted in a similar performance (Appendix A Fig. A1, Fig. A2). The RMSD for the independent test data was within ~1.5 µatm for Chl *a* (19.88 µatm), NPP (20.48 µatm) and NCP (21.68 µatm) and bias near zero.

Formatted: Font: Italic

The reduction in $p\mathrm{CO}_{2\ (\mathrm{sw})}$ RMSD that could be achieved if input parameter uncertainties were reduced to ~0 was assessed using the~~ previously described ~~perturbation analysis (Table 2, Appendix A Table A1). This showed that across the three training and validation datasets, satellite NCP uncertainties lead to a~~ n on average ~~36 % reduction in $p\mathrm{CO}_{2\ (\mathrm{sw})}$ RMSD, ~~with a~~ reduction of~~NPP a~~ 34 % for NPP ~~reduction ~~and ~~Chl *a* a ~~19 % reduction for Chl *a*~~., indicating that improving NCP uncertainties will have the largest impact on improving the estimated $p\mathrm{CO}_{2\ (\mathrm{sw})}$ fields. ~~The bias remained near zero for all parameters indicating good precision of the SA-FNN approach (not shown). Applying the Atlantic Meridional Transect *in situ* data as input to the SA-FNN and ~~resulting ~~using the perturbation analysis, a decrease in $p\mathrm{CO}_{2\ (\mathrm{sw})}$ RMSD of 25 % for NCP, 13 % for NPP and 7 % for Chl *a* was observed.

Formatted: Font: Italic

Formatted: Font: Italic

Formatted: Font: Italic

Formatted: Font: Italic

The reduction in $p\mathrm{CO}_{2\ (\mathrm{sw})}$ RMSD from reducing input parameter uncertainties by 10 % was also assessed through the perturbation analysis (Table 3). This indicated a decrease in $p\mathrm{CO}_{2\ (\mathrm{sw})}$ RMSD of 8 % for NCP, 5 % for NPP and 2 % for Chl *a*, again indicating that improving NCP uncertainties ~~will have~~has the largest impact on improving the estimated $p\mathrm{CO}_{2\ (\mathrm{sw})}$ fields.

Formatted: Font: Italic

Formatted: Font: Italic

Formatted: Font: Italic

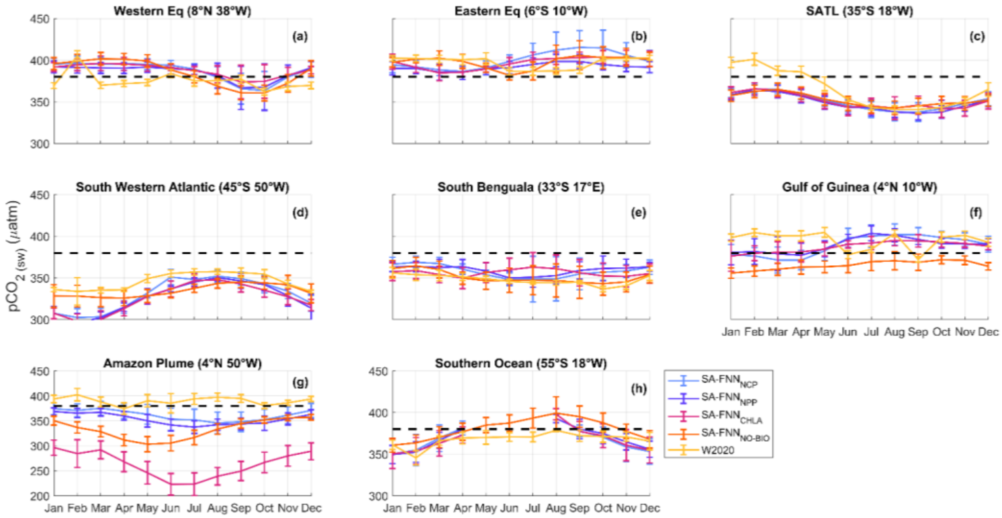
Western Eq (8°N 38°W)
(a)
Eastern Eq (6°S 10°W)
(b)
SATL (35°S 18°W)
(c)
South Western Atlantic (45°S 50°W)
(d)
South Benguala (33°S 17°E)
(e)
Gulf of Guinea (4°N 10°W)
(f)
Amazon Plume (4°N 50°W)
(g)
Southern Ocean (55°S 18°W)
(h)
pCO$_{2\,(sw)}$ (μatm)
450
400
350
300
250
200
Jan Feb Mar Apr May Jun Jul Aug Sep Oct Nov Dec
SA-FNN$_{NCP}$
SA-FNN$_{NPP}$
SA-FNN$_{CHLA}$
SA-FNN$_{NO-BIO}$
W2020

285

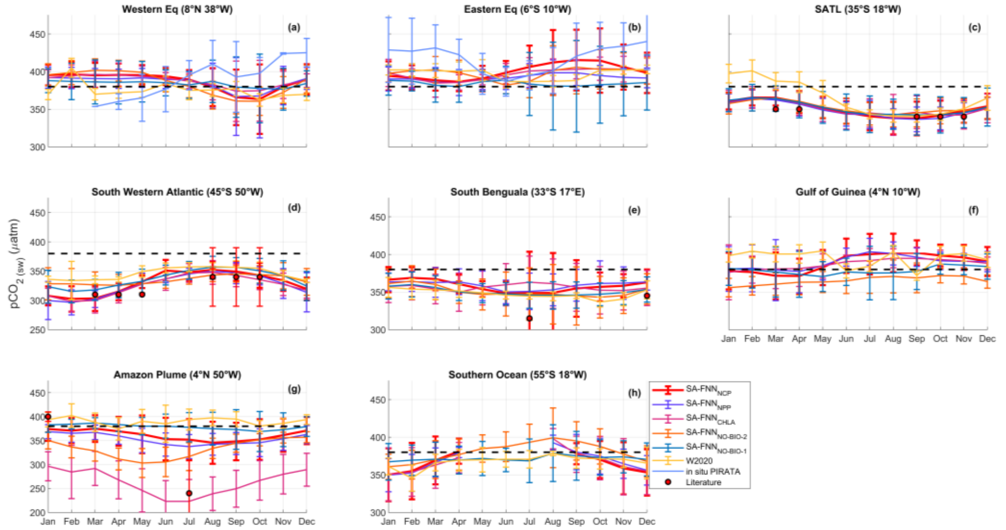

Fig. 3: Monthly climatologies of pCO$_{2\ (sw)}$ referenced to the year 2010 for the 8 stations marked in Fig. 1 from the SA-FNN$_{NCP}$, SA-FNN$_{NPP}$, SA-FNN$_{CHLA}$, SA-FNN$_{NO-BIO}$ and W2020 (Watson et al., 2020b). Light blue lines in Fig. 3a, b indicate the *in situ* pCO$_{2\ (sw)}$ observations from PIRATA buoys. The atmospheric CO$_2$ increase was set as 1.5 µatm yr^{-1}. Black dashed line indicates the atmospheric pCO$_2$ (~380 µatm). Error bars indicate the 2 standard deviation of the climatology (~95% interval), where larger error bars indicate a larger interannual variability. Red circles indicate the literature values of pCO$_{2\ (sw)}$ described in section 4.2. Note the different y-axis limits in Fig. 3g and Fig. 3d.

Formatted: Font: Italic

Formatted: Font: Italic

Formatted: Font: Italic

3.2. Comparison between~~of~~ SA-FNN$_{NCP}$ and~~with~~ other methods

The monthly climatology of pCO$_{2\ (sw)}$ generated using the SA-FNN$_{NCP}$ and referenced to the year 2010 showed differences with two published climatologies, especially in the Equatorial region (Appendix B). The monthly climatology for 8 stations (Fig. 1) were extracted from the SA-FNN$_{NCP}$, SA-FNN$_{NPP}$, SA-FNN$_{CHLA}$, SA-FNN$_{NO-BIO-1}$, SA-FNN$_{NO-BIO-2}$ and the W2020, to assess differences between the pCO$_{2\ (sw)}$ estimates (Fig. 3). The SA-FNN$_{NCP}$ and SA-FNN$_{NO-BIO-1}$ showed significant divergences in the Equatorial Atlantic (Figs. 3b, f, g; Fig. 4). At the eastern equatorial station, the interannual variability in pCO$_{2\ (sw)}$ from the SA-FNN$_{NCP}$ was high and a minimum occurred between January and April, which ~~slowly~~ gradually increased to a maximum in September and October (Fig. 3b). The SA-FNN$_{NO-BIO-1}$ showed ~~the opposite pattern, with a pCO$_{2\ (sw)}$ minima between May to July and a maxima for the remaining months with little interannual variability~~no seasonality in the pCO$_{2\ (sw)}$, and was consistently below the SA-FNN$_{NCP}$ pCO$_{2\ (sw)}$. The Gulf of Guinea station showed a similar variability

Formatted: Font: Italic

Formatted: Font: Italic

Formatted: Font: Italic

Formatted: Font: Italic

Formatted: Font: Italic

in the SA-FNN$_{\mathrm{NCP}}$ $p\mathrm{CO}_{2\,(\mathrm{sw})}$ except that the maxima was lower at this station (Fig. 3f). The SA-FNN$_{\mathrm{NO\text{-}BIO\text{-}1}}$ indicated $p\mathrm{CO}_{2\,(\mathrm{sw})}$ below the SA-FNN$_{\mathrm{NCP}}$ throughout the year. The greatest divergence occurred near the Amazon plume (Fig. 3g) where SA-FNN$_{\mathrm{NCP}}$ $p\mathrm{CO}_{2\,(\mathrm{sw})}$ was below or at $p\mathrm{CO}_{2\,(\mathrm{atm})}$ for all months and there was a large interannual variability in $p\mathrm{CO}_{2\,(\mathrm{sw})}$. The SA-FNN$_{\mathrm{NO\text{-}BIO\text{-}1}}$ displayed higher~~lower~~ $p\mathrm{CO}_{2\,(\mathrm{sw})}$ ~~between January and July~~ and a lower interannual variability (Fig. 3g).

The SA-FNN$_{\mathrm{NCP}}$ and SA-FNN$_{\mathrm{NO\text{-}BIO\text{-}1}}$ showed no significant difference in the seasonal patterns of $p\mathrm{CO}_{2\,(\mathrm{sw})}$ at stations south of 20 °S (Figs. 3c, d, e; Fig. 4). There was, however, a significant offset at some stations where the SA-FNN$_{\mathrm{NCP}}$ generally exhibited lower $p\mathrm{CO}_{2\,(\mathrm{sw})}$ in austral summer and a higher interannual variation. The SA-FNN$_{\mathrm{NCP}}$ was significantly different to the W2020 and SA-FNN$_{\mathrm{NO\text{-}BIO\text{-}2}}$ at similar stations as the SA-FNN$_{\mathrm{NO\text{-}BIO\text{-}1}}$ (Fig. 3, Fig. 4).

The SA-FNN$_{\mathrm{NCP}}$ and SA-FNN$_{\mathrm{CHLA}}$ showed significant differences in $p\mathrm{CO}_{2\,(\mathrm{sw})}$ values in the South Benguela and Amazon Plume. In the South Benguela (Fig. 3e; Fig. 4), SA-FNN$_{\mathrm{NCP}}$ ~~gave~~has ~~a~~ $p\mathrm{CO}_{2\,(\mathrm{sw})}$ maxima in austral summer, whereas the SA-FNN$_{\mathrm{CHL}}$ ~~maximum~~ maximum occurs~~red~~ in austral winter. In the Amazon Plume there was significant offset between the two methods and the SA-FNN$_{\mathrm{CHL}}$ ~~gave~~ resulted in lower $p\mathrm{CO}_{2\,(\mathrm{sw})}$ compared to the SA-FNN$_{\mathrm{NCP}}$ (Fig. 3g; Fig. 4). The SA-FNN$_{\mathrm{NCP}}$ and SA-FNN$_{\mathrm{NPP}}$ had a significant offset at the Eastern Equatorial station (Fig. 3c; Fig. 4), where the SA-FNN$_{\mathrm{NPP}}$ indicated lower $p\mathrm{CO}_{2\,(\mathrm{sw})}$. For the other stations, no significant differences were observed.

Formatted: Font: Italic

Formatted: Font: Italic

Formatted: Font: Italic

Formatted: Font: Italic

Formatted: Font: Italic

Formatted: Font: Italic

Formatted: Font: Italic

Formatted: Font: Italic

Formatted: Font: Italic

Formatted: Font: Italic

Formatted: Font: Italic

Formatted: Font: Italic

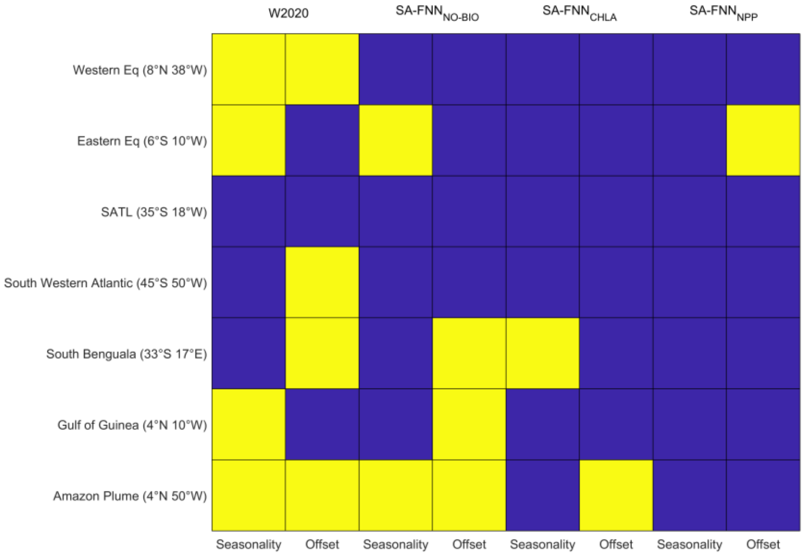
W2020
SA-FNN$_{NO-BIO}$
SA-FNN$_{CHLA}$
SA-FNN$_{NPP}$
Western Eq (8°N 38°W)
Eastern Eq (6°S 10°W)
SATL (35°S 18°W)
South Western Atlantic (45°S 50°W)
South Benguala (33°S 17°E)
Gulf of Guinea (4°N 10°W)
Amazon Plume (4°N 50°W)
Seasonality
Offset
Seasonality
Offset
Seasonality
Offset
Seasonality
Offset

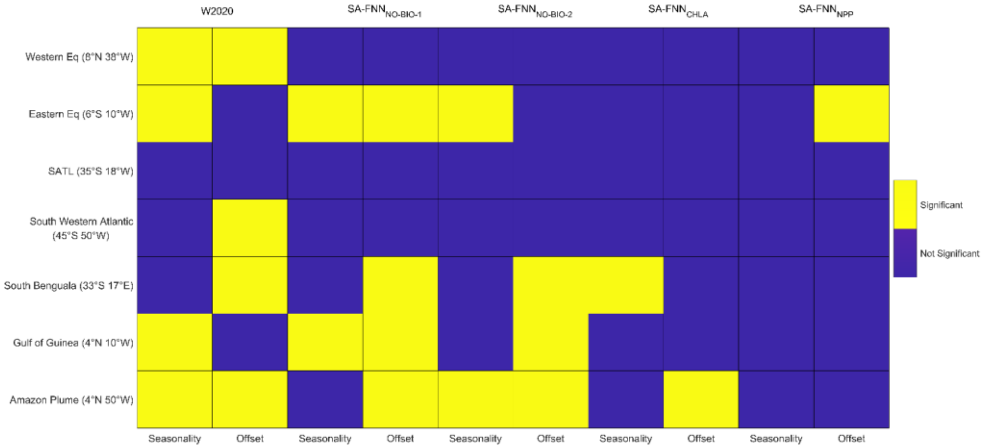
W2020
SA-FNN$_{NO-BIO-1}$
SA-FNN$_{NO-BIO-2}$
SA-FNN$_{CHLA}$
SA-FNN$_{NPP}$
Western Eq (8°N 38°W)
Eastern Eq (6°S 10°W)
SATL (35°S 18°W)
South Western Atlantic (45°S 50°W)
South Benguala (33°S 17°E)
Gulf of Guinea (4°N 10°W)
Amazon Plume (4°N 50°W)
Seasonality
Offset
Seasonality
Offset
Seasonality
Offset
Seasonality
Offset
Seasonality
Offset
Significant
Not Significant

Fig. 4: Statistical comparison of the SA-FNN$_{\text{NCP}}$ with the W2020, SA-FNN$_{\text{NO-BIO-1}}$, SA-FNN$_{\text{NO-BIO-2}}$, SA-FNN$_{\text{CHLA}}$ and SA-FNN$_{\text{NPP}}$ climatologies, where yellow blocks indicate a significant difference ($\alpha = 0.05$). Seasonality indicates a difference in the seasonal cycle and offset indicates a difference between the mean $p\text{CO}_{2\ \text{(sw)}}$ of the climatologies.

4. Discussion

4.1. Assessment of biological parameters to estimate $p\text{CO}_{2\ \text{(sw)}}$

In this paper, the differences in estimating $p\text{CO}_{2\ \text{(sw)}}$ using FFNs with satellite derived NCP, NPP or Chl *a* were assessed. The SA-FNN$_{\text{NCP}}$ had an overall accuracy (21.68 µatm; Fig. 2) that is consistent with other approaches that have been developed for the Atlantic (22.83 µatm; Landschützer et al., 2013), and slightly lower than the published global result of 25.95 µatm (Landschützer et al., 2014). Training the SA-FNN using Chl *a* or~~,~~ NPP~~-~~ showed comparable broad-scale accuracy to NCP~~or NCP, there was no overall improvement in the broad-scale accuracy of pCO$_{2\ \text{(sw)}}$ compared to literature values in the South Atlantic~~. When the uncertainties in the input parameters were investigated however, differences in the estimates of $p\text{CO}_{2\ \text{(sw)}}$ were apparent. The perturbation analysis indicated that up to a 36 % improvement in estimating $p\text{CO}_{2\ \text{(sw)}}$ could be achieved if NCP data uncertainties were reduced (Table 2). A similar improvement could be obtained if the NPP uncertainties were reduced (Table 2). Ford et al. (2021b) showed that up to 40 % of the uncertainty in satellite NCP is attributed to the uncertainty in satellite NPP, which is an input to the NCP approach. This suggests that improvements in estimating NPP from satellite data will lead to a further improvement in estimating $p\text{CO}_{2\ \text{(sw)}}$ from NCP. These improvements could be achieved through advances in the water column light field (e.g. Sathyendranath et al., 2020), better estimation of the vertical variability of input parameters or assignment of photosynthetic parameters (e.g. Kulk et al., 2020), for example. For a discussion on improving satellite NPP estimates we refer the reader to Lee et al. (2015).

~~Satellite NCP is reliant on NPP as input (Tilstone et al., 2015a; Ford et al., 2021), and NPP requires Chl *a* as the primary input (e.g. Lobanova et al., 2018; Platt et al., 1991; Tilstone et al., 2015b).~~ To uncouple the Chl *a*, NPP and NCP estimates and their uncertainties, the perturbation analysis was also conducted on Atlantic Meridional Transect *in situ* observations. This showed that reducing *in situ* NCP uncertainties provided the greatest reduction in $p\text{CO}_{2\ \text{(sw)}}$ RMSD, which was three times the reduction achievable using Chl *a* (Table 2; Table 3). This indicates that the optimal predictive power of Chl *a* to estimate $p\text{CO}_{2\ \text{(sw)}}$ has been reached and to achieve further improvements in estimates of $p\text{CO}_{2\ \text{(sw)}}$ and reduction in its associated uncertainty, requires the use of NCP.

A reduction of input uncertainties to ~0 is near impossible, but a reduction by 10 % could be feasible (e.g. NCP uncertainty reduced from 45 to 40.5 mmol O_2 m^{-2} d^{-1}; Table 1). A perturbation analysis conducted for this showed similar results, with NCP producing the greatest reduction in $p\text{CO}_{2\ \text{(sw)}}$ RMSD of 8 % compared to 2 % for Chl *a* (Table 3). Thus reducing NCP uncertainties will provide a greater improvement in $p\text{CO}_{2\ \text{(sw)}}$ compared to reducing the uncertainties in Chl *a*.

These improvements in estimating NCP could be achieved through many components. Ford et al. (2021b) showed 40 % of satellite NCP uncertainties were attributed to *in situ* NCP uncertainties. The *in situ* bottle incubation measurements could be improved using the principles of Fiducial Reference Measurements (FRM; Banks et al., 2020), which are traceable to

Formatted: Font: Italic

Formatted: Font: Italic

Formatted: Font: Italic

Formatted: Font: Italic

Formatted: Font: Italic

Formatted: Font: Italic

Formatted: Font: Italic

Formatted: Font: Italic

Formatted: Font: Italic

Formatted: Font: Italic

Formatted: Font: Italic

metrology standards, referenced to inter-comparison exercises, with a full uncertainty budget. This ~~however,~~ becomes complicated however, when considering the number of different methods to measure NCP and the large divergence between them (Robinson et al., 2009). A review of these methods has already been conducted (Duarte et al., 2013; Ducklow and Doney, 2013; Williams et al., 2013). The methods broadly fall into the following categories: a.) *in vitro* incubations of samples under light/dark treatments (Gist et al., 2009) and b.) *in situ* observations of oxygen to argon (O_2/Ar) ratios (Kaiser et al., 2005) or the observed isotopic signature of oxygen (Kroopnick, 1980; Luz and Barkan, 2000). All of these methods are subject to, but do not account for, the photochemical sink which may lead to underestimation of *in vitro* NCP by up to 22 % (Kitidis et al., 2014). Independent ground measurements that use accepted protocols for the *in vitro* method are currently made on the Atlantic Meridional Transect, however a community consensus should consider a consistent methodology for NCP. Increasing the number of such observations for the purpose of algorithm development, would further constrain the NCP, but also provide observations across the lifetime of newly launched satellites. The uncertainties on each *in vitro* measurement are assessed through replicate bottles which could be used to calculate a full uncertainty budget for each NCP measurement when combined with analytical uncertainties.

Serret et al. (2015) indicated that NCP is controlled by both the heterogeneity in NPP and respiration. The satellite NCP algorithm applied in this study accounts for some of the heterogeneity in respiration, through an empirical SST to NCP relationship (Tilstone et al., 2015a). Quantifying the variability in respiration could further improve NCP estimates when coupled with NPP rates from satellite observations.

4.2. Accuracy of SA-FNN$_{\mathrm{NCP}}$ $p\mathrm{CO}_{2\,(\mathrm{sw})}$ at seasonal and interannual scales

The seasonal and interannual variability of $p\mathrm{CO}_{2\,(\mathrm{sw})}$ estimated using the SA-FNN$_{\mathrm{NCP}}$ was compared with the SA-FNN$_{\mathrm{NO\text{-}BIO}}$, W2020 (Watson et al., 2020b), SA-FNN$_{\mathrm{CHL}}$ and SA-FNN$_{\mathrm{NPP}}$ at 8 stations. The stations (Fig. 1) represent locations of previous studies into *in situ* $p\mathrm{CO}_{2\,(\mathrm{sw})}$ variability ~~in the South Atlantic Ocean and~~allowing ~~allow~~ comparisons with literature values. Significant differences between the SA-FNN$_{\mathrm{NCP}}$ and SA-FNN$_{\mathrm{NO\text{-}BIO}}$ were observed at four stations (Fig. 4), especially in the Equatorial Atlantic.

At 8° N 38° W (Fig. 3a), Lefèvre et al. (2020) reported $p\mathrm{CO}_{2\,(\mathrm{sw})}$ to be stable at ~400 µatm, between June and August 2013, and to decrease in September to ~360 µatm, which is attributed to the Amazon Plume propagating into the western Equatorial Atlantic (Coles et al., 2013). Bruto et al. (2017) indicated however, that elevated $p\mathrm{CO}_{2\,(\mathrm{sw})}$ at ~430 µatm exist ~~throughout the year~~ from 2008 to 2011. The PIRATA buoy $p\mathrm{CO}_{2\,(\mathrm{sw})}$ observations (Fig. 3a) clearly highlight the differences between these years, but there are less than 4 years of monthly observations available, and do not resolve the full seasonal cycle. For the station in the Amazon Plume at 4° N 50° W (Fig. 3g), where the effects of the plume extend northwest towards the Caribbean (Coles et al., 2013; Varona et al., 2019), Lefèvre et al. (2017) indicated that this region acts as a sink for CO_2 ($p\mathrm{CO}_{2\,(\mathrm{sw})} < p\mathrm{CO}_{2\,(\mathrm{atm})}$), especially between May to July, coincident with maximum discharge from the Amazon River (Dai and Trenberth, 2002). Valerio et al. (2021) indicated $p\mathrm{CO}_{2\,(\mathrm{sw})}$ varied at~~above~~ and below $p\mathrm{CO}_{2\,(\mathrm{atm})}$ at 4° N 50° W consistent with the SA-FNN$_{\mathrm{NCP}}$. The interannual variability of $p\mathrm{CO}_{2\,(\mathrm{sw})}$ has been shown to be high in this region in all

Formatted: Font: Italic

Formatted: Font: Italic

Formatted: Font: Italic

Formatted: Font: Italic

Formatted: Font: Italic

Formatted: Font: Italic

Formatted: Font: Italic

Formatted: Font: Italic

Formatted: Font: Italic

Formatted: Font: Italic

Formatted: Font: Italic

months (Lefèvre et al., 2017). The SA-FNN$_{NCP}$ provided a better representation of the seasonal and interannual variability induced by the Amazon River discharge and associated plume at these two stations compared to the SA-FNN$_{NO-BIO}$, although differences were small at 8° N 38° W.

The station in the Eastern Tropical Atlantic at 6° S 10° W (Fig. 3b), is under the influence of the equatorial upwelling (Lefèvre, Guillot, Beaumont, & Danguy, 2008), which is associated with the upwelling of CO_2 rich waters between June and September. Lefèvre et al. (2008) indicated that peak $pCO_{2\,(sw)}$ of ~440 µatm was observed in September, and remained stable until December, before decreasing to a minima of ~360 µatm in May (Parard et al., 2010). Lefèvre et al. (2016) showed however, that the influence of the equatorial upwelling does not reach the buoy in all years, and in some years lower $pCO_{2\,(sw)}$ is observed. The PIRATA buoy observations (Fig. 3b) clearly show this seasonality but also highlight the interannual variability in *in situ* $pCO_{2\,(sw)}$. Further north ~~at the station~~ at 4° N 10° W (Fig. 3f), Koffi et al. (2010) suggested that this region follows a similar seasonal cycle as the station at 6° S 10° W, but that $pCO_{2\,(sw)}$ is ~30 µatm lower (Koffi et al., 2016). The interannual variability in SA-FNN$_{NCP}$ $pCO_{2\,(sw)}$ clearly shows the influence of the equatorial upwelling at these stations, with latitudinal gradients in $pCO_{2\,(sw)}$ during the upwelling period (Lefèvre et al., 2016), but struggles to identify elevated $pCO_{2\,(sw)}$ between December to April shown by the PIRATA buoy observations (Fig. 3b).~~.~~ By contrast, the SA-FNN$_{NO-BIO-1}$ indicated little influence from the equatorial upwelling~~, little interannual variability,~~ and a depressed $pCO_{2\,(sw)}$ during the upwelling season.

The two methods converge on the seasonal cycle at the remaining stations although significant offsets in the mean annual $pCO_{2\,(sw)}$ remain. The station at 35° S 18° W (Fig. 3c) has consistently been implied as a sink for CO_2. Lencina-Avila et al. (2016) showed the region to have 340 µatm $pCO_{2\,(sw)}$ ~~at 340 µatm~~ and to be a sink for CO_2 between October to December. Similarly, Kitidis et al. (2017) implied that the region is a sink for CO_2 during March to April. The region has depressed $pCO_{2\,(sw)}$ due to high biological activity that originates from the Patagonian shelf and the South Subtropical Convergence Zone. The station at 45° S 50° W (Fig. 3d), has also been implied as a strong, but highly variable sink, where $pCO_{2\,(sw)}$ can be between ~280 µatm and ~380 µatm during austral spring, and is constant at ~310 µatm during austral autumn (Kitidis et al., 2017). The SA-FNN$_{NCP}$ and SA-FNN$_{NO-BIO-1}$ methods reproduced the seasonal variability in the $pCO_{2\,(sw)}$ at these two stations accurately, but only the SA-FNN$_{NCP}$ captures the magnitude of the depressed $pCO_{2\,(sw)}$ at 45° S.

Within the southern Benguela upwelling system, $pCO_{2\,(sw)}$ at ~~the~~ station 33° S 17° E (Fig. 3e) is influenced by gradients in the seasonal upwelling (Hutchings et al., 2009). Santana-Casiano et al. (2009) showed that $pCO_{2\,(sw)}$ varies from ~310 µatm in July to ~340 µatm in December and that the region is a CO_2 sink through the year. González-Dávila et al. (2009) suggested however, that this CO_2 sink is highly variable during upwelling events, and that recently upwelled waters act as a source ($pCO_{2\,(sw)} > pCO_{2\,(atm)}$) of CO_2 to the atmosphere (Gregor and Monteiro, 2013). Arnone et al. (2017) indicated elevated $pCO_{2\,(sw)}$ during austral spring and autumn at the station, with a ~40 µatm seasonal cycle amplitude The SA-FNN$_{NCP}$ and SA-FNN$_{NO-BIO-1}$ were able to reproduce the seasonal cycle, although the SA-FNN$_{NCP}$ correctly represented the seasonal ~~differences~~ magnitude in $pCO_{2\,(sw)}$ as reported by Santana-Casiano et al. (2009) and Arnone et al. (2017).~~.~~

Formatted: Font: Italic
Formatted: Font: Italic
Formatted: Font: Italic
Formatted: Font: Italic
Formatted: Font: Italic
Formatted: Font: Italic
Formatted: Font: Italic
Formatted: Font: Italic
Formatted: Font: Italic
Formatted: Font: Italic
Formatted: Font: Italic
Formatted: Font: Italic
Formatted: Font: Italic
Formatted: Font: Italic
Formatted: Font: Italic
Formatted: Font: Italic
Formatted: Font: Italic
Formatted: Font: Italic
Formatted: Font: Italic
Formatted: Font: Italic
Formatted: Font: Italic

In summary, for these stations,~~Overall, compared to the SA-FNN$_{NO-BIO}$ at these stations, ~~ the SA-FNN$_{NCP}$ better represents the seasonality and the interannual variability of pCO$_{2\ (sw)}$ in the South Atlantic Ocean compared to the SA-FNN$_{NO-BIO-1}$, especially in the Equatorial Atlantic. The SA-FNN$_{NO-BIO-2}$ also displayed significant differences to SA-FNN$_{NCP}$, indicating that the variability in pCO$_{2\ (sw)}$ has a strong biological contribution which is not fully represented and explained by the additional physical parameters included in the FNN. The SA-FNN$_{NO-BIO-2}$ and W2020 both displayed significant differences to the SA-FNN$_{NCP}$ at ~~similar~~specific stations (Fig. 4)~~, although their pCO$_{2\ (sw)}$ estimates were not always consistent~~There are methodological differences between these approaches ~~. The~~however. The SA-FNN method uses only *in situ* pCO$_{2\ (sw)}$ observations from the South Atlantic Ocean to train the FNNs. The W2020 uses global *in situ* pCO$_{2\ (sw)}$ observations to train FNNs for 16 provinces with similar seasonal cycles (Landschützer et al., 2014; Watson et al., 2020b). The W2020 will therefore be weighted to pCO$_{2\ (sw)}$ variability in regions of relatively abundant *in situ* observations (i.e. Northern Hemisphere) and may not be fully representative of the South Atlantic Ocean. This would explain the SA-FNN$_{NO-BIO-2}$ and W2020 differences, when driven using the same input variables.

Comparing the SA-FNN$_{NCP}$ and SA-FNN$_{CHLA}$ there were two significant differences (Fig. 4). A difference in the seasonal cycle in the southern Benguela (Fig. 3e) was observed. Santana-Casiano et al. (2009) showed that the minima pCO$_{2\ (sw)}$ in July and maxima in December, consistent with the SA-FNN$_{NCP}$ and SA-FNN$_{NPP}$ whereas the SA-FNN$_{CHL}$ estimated the opposite scenario. Lamont et al. (2014) reported Chl *a* concentrations to remain consistent in May and October, but NPP rates were significantly higher in October, associated with increased surface PAR and enhanced upwelling.~~,~~ The disconnect between Chl *a*~~,~~ and NPP~~ and NCP~~ can also be observed in the satellite observations (Appendix C Fig. C1) limiting~~s~~ the ability of Chl *a* to estimate pCO$_{2\ (sw)}$, which is highlighted by the failure of the SA-FNN$_{CHLA}$ to identify the seasonal pCO$_{2\ (sw)}$ cycle.

A Chl *a* to NPP disconnect~~, due to light limitation caused by suspended sediments,~~ has also been reported in the Amazon Plume (Smith and Demaster, 1996), where Chl *a* concentrations can be similar but NPP rates significantly different due to light limitation caused by suspended sediments.~~ where a~~ A significant offset between the SA-FNN$_{NCP}$ and SA-FNN$_{CHLA}$ was observed in this region (Fig. 3g; Fig. 4). Lefèvre et al. (2017) reported pCO$_{2\ (sw)}$ values ranging from 400 ± ~10 µatm in January to ~240 ± ~70 µatm in May. Although, the SA-FNN$_{NCP}$ January estimates are consistent, the May estimates are higher than these *in situ* ~~observations~~measurements. These observations were made further north (6° N) where the turbidity within the plume has decreased sufficiently for irradiance to elevate NPP rates (Smith and Demaster, 1996), which decrease pCO$_{2\ (sw)}$. Chl *a* remains relatively consistent across the plume (not shown), suggesting a disconnect between Chl *a* and NPP at 4° N 50° W which would lead to lower pCO$_{2\ (sw)}$ estimates by the SA-FNN$_{CHLA}$, where NPP rates are low due to light limitation (Chen et al., 2012; Smith and Demaster, 1996). Respiration would be elevated from the decomposition of riverine organic material reducing NCP further (Cooley et al., 2007; Jiang et al., 2019; Lefèvre et al., 2017). It is noted that the Amazon Plume is a dynamic region with transient, localised biological and pCO$_{2\ (sw)}$ features (Cooley et al., 2007; Ibánhez et al., 2015; Lefèvre et al., 2017; Valerio et al., 2021) that may be masked by the coarse resolution of estimates available using

Formatted: Font: Italic

Formatted: Font: Italic

Formatted: Font: Italic

Formatted: Font: Italic

Formatted: Font: Italic

Formatted: Font: Italic

Formatted: Font: Italic

Formatted: Font: Italic

Formatted: Font: Italic

Formatted: Font: Italic

Formatted: Font: Italic

Formatted: Font: Italic

Formatted: Font: Italic

satellite data. The SA-FNN$_{NCP}$ however, agreed with *in situ* $p\mathrm{CO}_{2\,(sw)}$ observations at 4° N 50° W where $p\mathrm{CO}_{2\,(sw)}$ varied ~~above~~ at ~~and~~ or below $p\mathrm{CO}_{2\,(atm)}$ (Valerio et al., 2021).

Though the differences between the SA-FNN$_{NCP}$ and SA-FNN$_{CHLA}$ may appear small, the Amazon Plume and Benguela Upwelling have a higher intensity in the CO_2 flux per unit area compared to the open ocean, illustrating a disproportionate contribution to the overall global CO_2 sink than their small areal coverage implies (Laruelle et al., 2014). The differences in the $p\mathrm{CO}_{2\,(sw)}$ estimates result in a 22 Tg C yr^{-1} alteration in the annual CO_2 flux for the South Atlantic Ocean (SA-FNN$_{NCP}$ = +14 Tg C yr^{-1}; SA-FNN$_{CHLA}$ = -9 Tg C yr^{-1}; Fig. 5f). This unequivocally reinforces the use of NCP to improve basin scale estimates of $p\mathrm{CO}_{2\,(sw)}$, especially in regions where Chl *a*, NPP and NCP become disconnected.

Recent assessments of the strength of the global oceanic CO_2 sink have been made using $p\mathrm{CO}_{2\,(sw)}$ fields estimated using no biological parameters as input (Watson et al., 2020b). Our results indicate that the SA-FNN$_{NCP}$ more accurately represented the $p\mathrm{CO}_{2\,(sw)}$ variability in the South Atlantic Ocean compared to the SA-FNN$_{NO\text{-}BIO\text{-}2}$, which included additional physical parameters. Estimating the South Atlantic Ocean net CO_2 flux with the SA-FNN$_{NCP}$ $p\mathrm{CO}_{2\,(sw)}$ produced a 14 Tg C yr^{-1} source compared to a 10 Tg C yr^{-1} sink indicated by the SA-FNN$_{NO\text{-}BIO\text{-}2}$ (Fig. 5f). The incremental inclusion of parameters to ~~properly~~ account for the biological signal starting with Chl *a* (-9 Tg C yr^{-1}) then~~o~~ NPP (-7 Tg C yr^{-1}) then~~o~~ NCP (+14 Tg C yr^{-1}) switched the South Atlantic Ocean from a CO_2 sink to a source, which is driven by differences in the $p\mathrm{CO}_{2\,(sw)}$ estimates in regions that are biologically controlled~~, such as the Equatorial Atlantic~~. This 21 Tg C yr^{-1} difference between the SA-FNN$_{NCP}$ and SA-FNN$_{NPP}$ is due to additional outgassing in the Equatorial Atlantic provinces of the WTRA and ETRA (Fig 1a; Fig.5f). Compared to the *in situ* $p\mathrm{CO}_{2\,(sw)}$ observations at the Equatorial stations (Fig. 3a, b), it is likely that the outgassing is still underestimated by the SA-FNN$_{NCP}$ but does improve these estimates within the upwelling season (June – September).

Formatted: Font: Italic

Formatted: Font: Italic

Formatted: Font: Italic

Formatted: Font: Italic

Formatted: Font: Italic

Formatted: Font: Italic

Formatted: Font: Italic

Formatted: Font: Italic

Formatted: Font: Italic

Formatted: Subscript

Formatted: Subscript

Formatted: Font: Italic

Formatted: Font: Italic

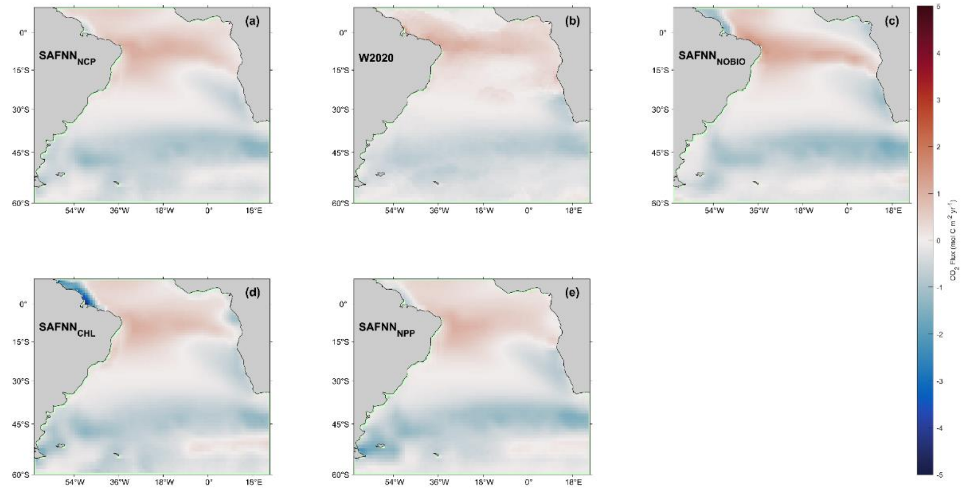
(a)
SAFNN$_{NCP}$
(b)
W2020
(c)
SAFNN$_{NOBIO}$
(d)
SAFNN$_{CHL}$
(e)
SAFNN$_{NPP}$
0°
15°S
30°S
45°S
60°S
54°W
36°W
18°W
0°
18°E
5
4
3
2
1
0
-1
-2
-3
-4
-5
CO$_2$ Flux (mol C m^{-2} yr^{-1})

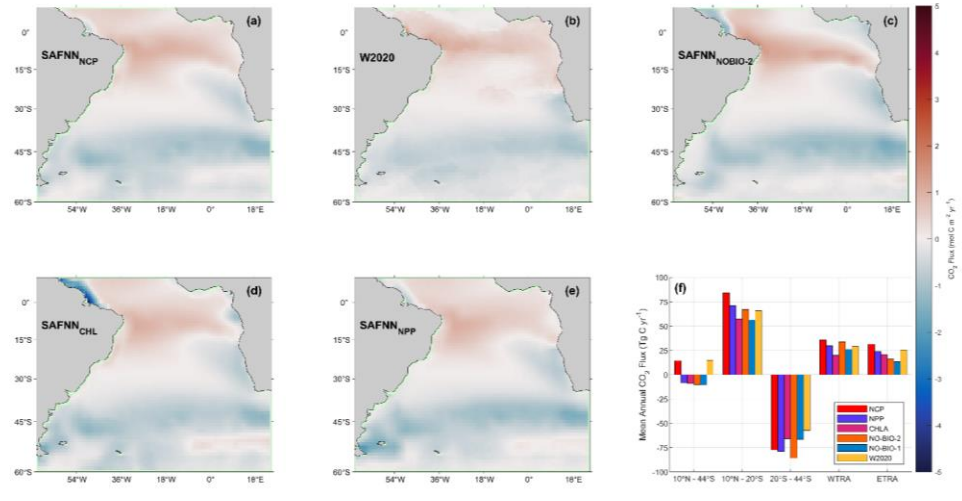
(a)
SAFNN$_{NCP}$
(b)
W2020
(c)
SAFNN$_{NOBIO-2}$
(d)
SAFNN$_{CHL}$
(e)
SAFNN$_{NPP}$
(f)
0°
15°S
30°S
45°S
60°S
54°W
36°W
18°W
0°
18°E
Mean Annual CO$_2$ Flux (Tg C yr^{-1})
100
75
50
25
0
-25
-50
-75
-100
10°N - 44°S
10°N - 20°S
20°S - 44°S
WTRA
ETRA
NCP
NPP
CHLA
NO-BIO-2
NO-BIO-1
W2020
5
4
3
2
1
0
-1
-2
-3
-4
-5
CO$_2$ Flux (mol C m^{-2} yr^{-1})

Fig. 5: Long term average annual mean CO_2 flux for the South Atlantic Ocean, using $pCO_{2\,(sw)}$ estimates from (a) SA-FNN$_{NCP}$, (b) W2020 (Watson, et al., 2020a), (c) SA-FNN$_{NOBIO}$~~-2~~, (d) SA-FNN$_{CHLA}$ and (e) SA-FNN$_{NPP}$. (f) Bar chart displaying the mean annual CO_2 flux for different regions of the South Atlantic Ocean including 10° N to 44° S (Whole South Atlantic Ocean), 10° N to 20° S, 20° S to 44° S, alongside the WTRA and ETRA biogeochemical provinces (Fig. 1a).

Formatted: Font: Italic

The W2020 identified the South Atlantic Ocean as a source for CO_2 of 15 Tg C yr^{-1}, which is ~~source for CO_2~~ consistent with the SA-FNN$_{NCP}$ (Fig. 5f). The SA-FNN$_{NCP}$ however, indicated the Equatorial Atlantic (10° N to 20° S) as a 20 Tg C yr^{-1} stronger source and south of 20° S (20° S to 44° S) as a 20 Tg C yr^{-1} stronger sink. These differences indicate that biologically induced variability in $pCO_{2\,(sw)}$ would not be captured by the W2020 and could~~may~~ reduce the variability in the global ocean CO_2 sink.~~ reinforcing the improvement that NCP provides~~. A further SA-FNN trained with $pCO_{2\,(atm)}$, SST, salinity, mixed layer depth and NCP indicated a similar CO_2 source of 12 Tg C yr^{-1} (data not shown) as the SA-FNN$_{NCP}$ for the South Atlantic Ocean, highlighting that additional physical parameters cannot fully account for the biological contribution to the variability in $pCO_{2\,(sw)}$. This further confirms the importance of using NCP within estimates of the global ocean CO_2 sink.

Formatted: Font: Italic

5. Conclusions

In this paper, we compare neural network models of $pCO_{2\,(sw)}$ parameterised separately using either satellite ~~using three biological proxies,~~ Chl *a*, NPP or NCP as biological proxies. ~~available from earth observation data to train a neural network scheme to estimate $pCO_{2\,(sw)}$.~~ The results suggest that using NCP improved the estimation of $pCO_{2\,(sw)}$. The differences between satellite Chl *a*, NPP or NCP were initially small, but the use of a perturbation analysis to ~~account~~ assess the~~for~~ uncertainties in these parameters, showed that NCP has a~~the~~ greater~~st~~ potential uncertainty reduction ~~reduction in $pCO_{2\,(sw)}$ uncertainty~~ of up to ~36 % of the RMSD, compared to a ~19 %~~ reduction~~ for Chl *a*. These results were verified using *in situ* observations from the Atlantic Meridional Transect, which resulted in a 25 % improvement in $pCO_{2\,(sw)}$ RMSD when the *in situ* NCP uncertainties were~~are~~ reduced, compared to 7 % for Chl *a* and 13 % for NPP. ~~Practical approaches to reduce the uncertainties in both the *in situ* and satellite NCP observations are discussed.~~

Formatted: Font: Italic

Formatted: Font: Italic

Monthly climatological estimates of $pCO_{2\,(sw)}$ at 8 stations in the South Atlantic Ocean, calculated using satellite NCP were compared with the NPP and the Chl *a* approaches and two ~~a baseline approach~~ that do~~es~~ not use biological parameters~~, at 8 stations in the South Atlantic Ocean~~. The NCP approach significantly improved on both~~the baseline~~ approaches with no biological parameters at 4 stations in reconstructing the seasonal and interannual variability, compared to *in situ* $pCO_{2\,(sw)}$ observations. At the remaining 4 stations, differences were also observed although these were not statistically significant. In the eastern Equatorial Atlantic, in the upwelling region, ~~A~~a significant difference between the NCP and NPP approaches ~~occurred in the eastern Equatorial Atlantic, in the equatorial upwelling region~~. Significant differences between the NCP and Chl *a* approaches were also observed in the Benguela upwelling and Amazon Plume, where $pCO_{2\,(sw)}$ from Chl *a* suggested that photosynthetic rates were not solely controlled by Chl *a*. Using NCP to estimate $pCO_{2\,(sw)}$ ~~estimated from NCP identified~~

Formatted: Font: Italic

Formatted: Font: Italic

Formatted: Font: Italic

Formatted: Font: Italic

the South Atlantic Ocean was characterised as a net source of CO_2, whereas methods that only include physical controls have indicated the region~~it~~ to be a small sink for CO_2. Sequentially using ~~firstly~~ Chl *a* to estimate $pCO_{2\ (sw)}$, then NPP incrementally reduced the South Atlantic CO_2 sink and finally using NCP ~~switched~~ the area switched to being a source of CO_2. These results indicate that in regions where biological activity is important in controlling the variability in $pCO_{2\ (sw)}$, the use of NCP, which is available from satellite data, is important for quantifying the ocean carbon pump, and for providing data in areas that are sparsely covered by observations such as the Southern Ocean.

Formatted: Font: Italic

Formatted: Font: Italic

Appendices

Appendix A - Feed forward neural network training and perturbation analysis

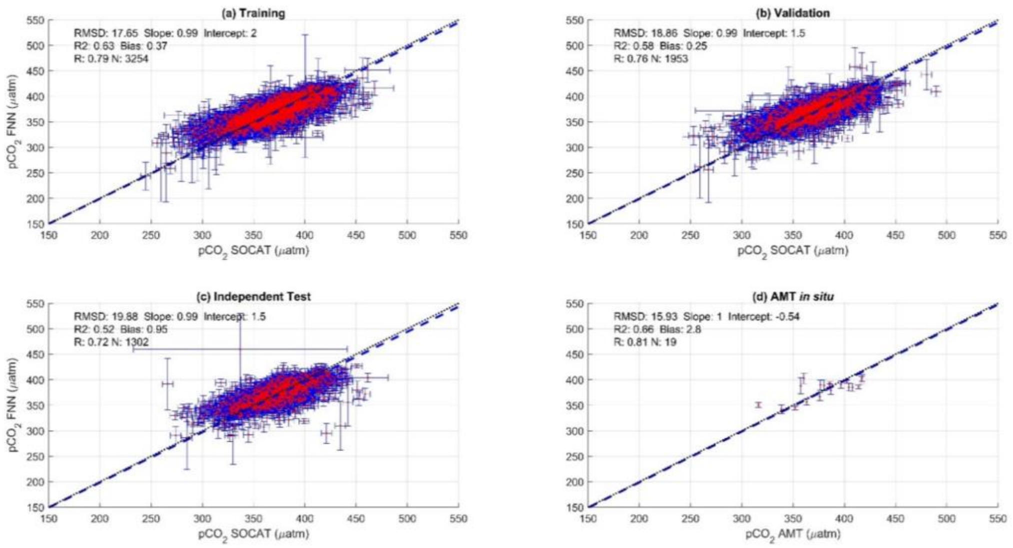

Fig. A1: Scatter plots showing the combined performance of the 8 feed forward neural networks trained using chlorophyll a for 4 separate training and validation datasets; (a) Training, (b) Validation, (c) Independent Test and (d) Atlantic Meridional Transect (AMT) in situ. The blue dashed line is the Type II regression and the black dashed line is the 1:1 line. Horizontal error bars indicate the uncertainty of the SOCATv2020 *p*CO_2 (sw). Vertical error bars indicate the uncertainty attributed to the input parameter uncertainty propagated through the feed forward neural networks. The statistics within each plot are; Root Mean Square Difference (RMSD), Slope and Intercept of the Type II regression, Coefficient of Determination (R2), Pearson's Correlation Coefficient (R), Bias and number of samples (N).

Formatted: Font: Italic

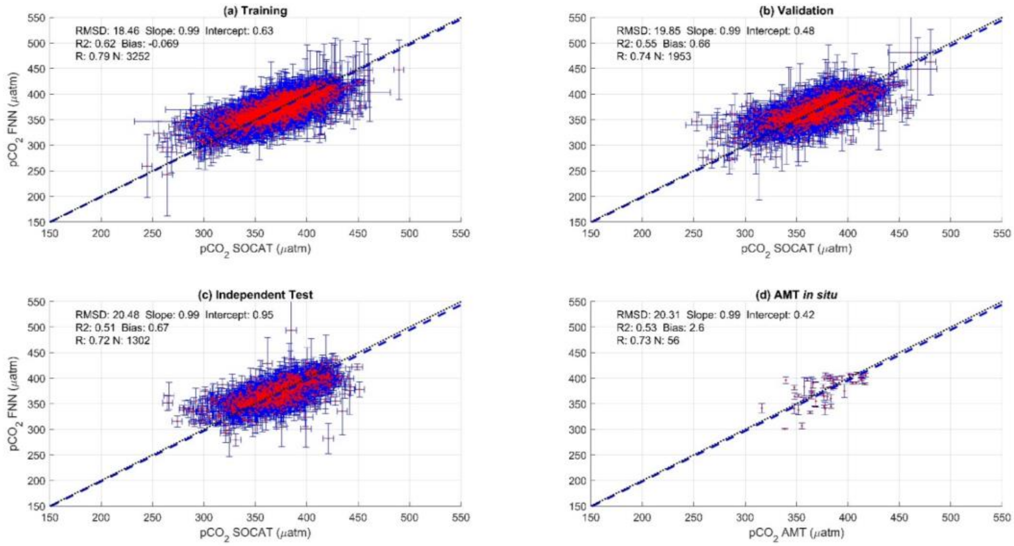

Fig. A2: Scatter plots showing the combined performance of the 8 feed forward neural networks trained using net primary production for 4 separate training and validation datasets; (a) Training, (b) Validation, (c) Independent Test and (d) Atlantic Meridional Transect (AMT) in situ. The blue dashed line is the Type II regression and the black dashed line is the 1:1 line. Horizontal error bars indicate the uncertainty of the SOCATv2020 $p\mathrm{CO}_{2\,(sw)}$. Vertical error bars indicate the resulting uncertainty attributed to the input parameter uncertainty propagated through the feed forward neural networks. The statistics within each plot are; Root Mean Square Difference (RMSD), Slope and Intercept of the Type II regression, Coefficient of Determination (R2), Pearson's Correlation Coefficient (R), Bias and number of samples (N).

Formatted: Font: Italic

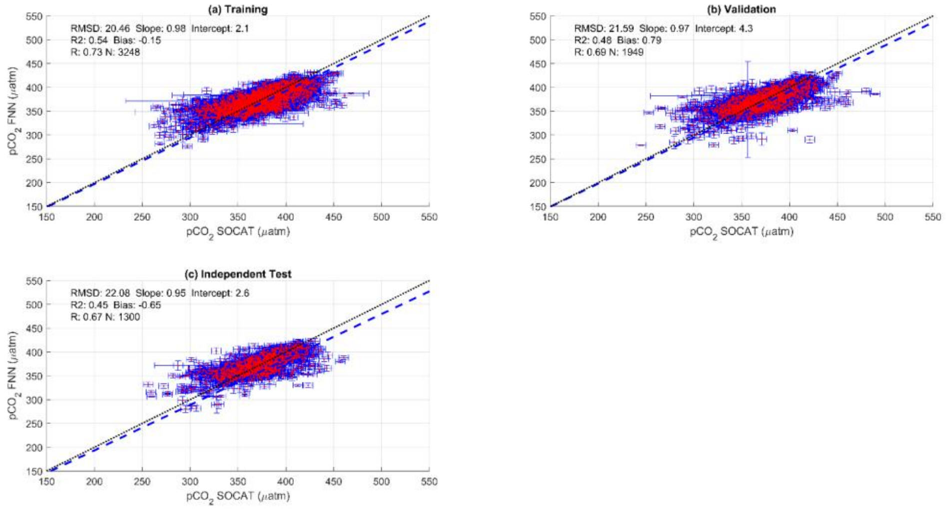

Fig. A3: Scatter plots showing the combined performance of the 8 feed forward neural networks trained using no biological parameters (SA-FNN$_{NO\text{-}BIO\text{-}1}$) for 3 separate training and validation datasets; (a) Training, (b) Validation and (c) Independent Test. The blue dashed line is the Type II regression and the black dashed line is the 1:1 line. Horizontal error bars indicate the uncertainty of the SOCATv2020 *p*CO$_{2\ (sw)}$. Vertical error bars indicate the resulting uncertainty attributed to the input parameter uncertainty propagated through the feed forward neural networks. The statistics within each plot are; Root Mean Square Difference (RMSD), Slope and Intercept of the Type II regression, Coefficient of Determination (R2), Pearson's Correlation Coefficient (R), Bias and number of samples (N).

Formatted: Normal

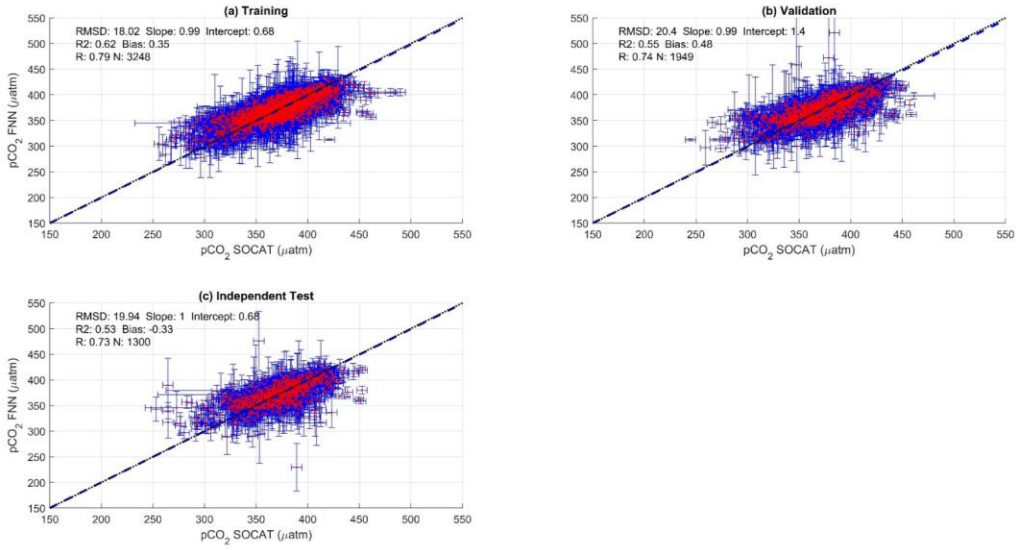

Fig. A4~~3~~: Scatter plots showing the combined performance of the 8 feed forward neural networks trained using no biological parameters (SA-FNN$_{NO-BIO-2}$) for 3 separate training and validation datasets; (a) Training, (b) Validation and (c) Independent Test. The blue dashed line is the Type II regression and the black dashed line is the 1:1 line. Horizontal error bars indicate the uncertainty of the SOCATv2020 *p*CO$_{2\ (sw)}$. Vertical error bars indicate the resulting uncertainty attributed to the input parameter uncertainty propagated through the feed forward neural networks. The statistics within each plot are; Root Mean Square Difference (RMSD), Slope and Intercept of the Type II regression, Coefficient of Determination (R2), Pearson's Correlation Coefficient (R), Bias and number of samples (N).

Formatted: Font: Italic

Table A1: The percentage reduction in Root Mean Square Difference (RMSD) attributable to the uncertainties in the input parameter for each training and validation datasets determined from a perturbation analysis as described in Sect. 2.5.

	Parameter	Training	Validation	Independent Test	AMT *in situ*
NCP	ALL	33 %	42 %	38 %	28 %
	SST	10 %	12 %	10 %	0.5 %
	Net Community Production	32 %	40 %	36 %	25 %
	$p\mathrm{CO}_{2\,\mathrm{(atm)}}$	6 %	7 %	6 %	9 %
Net Primary Production	ALL	34 %	40 %	40 %	17 %
	SST	9 %	10 %	10 %	0.4 %
	Net Primary Production	31 %	37 %	36 %	13 %
	$p\mathrm{CO}_{2\,\mathrm{(atm)}}$	6 %	6 %	6 %	9 %
Chlorophyll *a*	ALL	22 %	26 %	25 %	29 %
	SST	9 %	10 %	9 %	0.4 %
	Chlorophyll *a*	17 %	21 %	20 %	7 %
	$p\mathrm{CO}_{2\,\mathrm{(atm)}}$	8 %	9 %	9 %	16 %

Formatted: Font: Italic

Formatted: Font: Italic

Formatted: Font: Italic

Appendix B - Climatology comparison

A monthly climatology was generated from the SA-FNN$_{\mathrm{NCP}}$ monthly timeseries (Fig. B1), referenced to the year 2010, assuming an atmospheric CO_2 increase of 1.5 µatm yr^{-1} (Takahashi et al., 2009; Zeng et al., 2014). The standard deviation of the monthly climatology was computed, as an indication of the interannual variations in the climatology. The ability of the SA-FNN$_{\mathrm{NCP}}$ to estimate the spatial distribution of $p\mathrm{CO}_{2\,\mathrm{(sw)}}$ was compared to two methods.

Formatted: Font: Italic

Firstly, the SA-FNN$_{\mathrm{NCP}}$ climatology was compared to the climatology from Woolf et al. (2019), produced following the statistical 'ordinary block kriging' approach described in Goddijn-Murphy et al. (2015), using the SOCATv4 reanalysed data. The method provides an interpolation uncertainty where in regions of sparse data this becomes larger. Fig. B2 shows the methods produce similar climatological $p\mathrm{CO}_{2\,\mathrm{(sw)}}$ values for the South Atlantic Ocean, with some clear differences along the African coastline, and equatorial region.

Formatted: Font: Italic

Secondly, the SA-FNN$_{\mathrm{NCP}}$ was compared to a climatology calculated from the 'standard method', a Self Organising Map Feed Forward Neural Network presented in Watson et al. (2020b; W2020). Fig. B3 shows the methods produce similar climatological *p*CO$_{2\text{ (sw)}}$ values for the South Atlantic Ocean, however, clear differences in the Equatorial region occur across all months. In the central South Atlantic Ocean, artefacts form the self organising map can be seen during January and February.

Formatted: Font: Italic

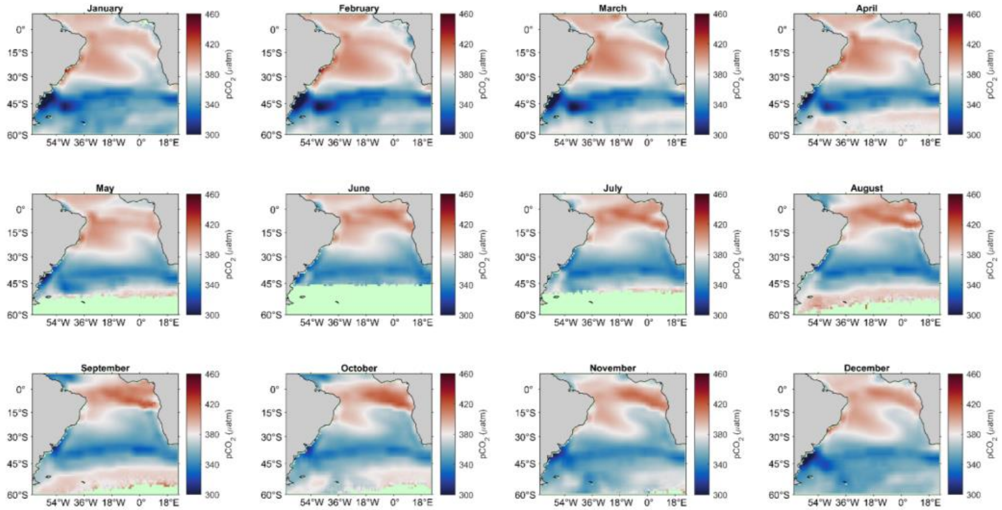

Fig. B1: Monthly climatologies of *p*CO$_{2\text{ (sw)}}$ between July 2002 and December 2018 estimated by the SA-FNN$_{\text{NCP}}$ approach referenced to 2010. The atmospheric CO$_2$ increase was set as 1.5 µatm yr^{-1}. The colour scale is centred on the atmospheric concentration for 2010 (~380 µatm). Red shaded areas indicate oversaturated regions, and blue shaded areas indicate under saturated regions. Light green areas indicate where no input data to compute *p*CO$_{2\text{ (sw)}}$ are available.

Formatted: Font: Italic

Formatted: Font: Italic

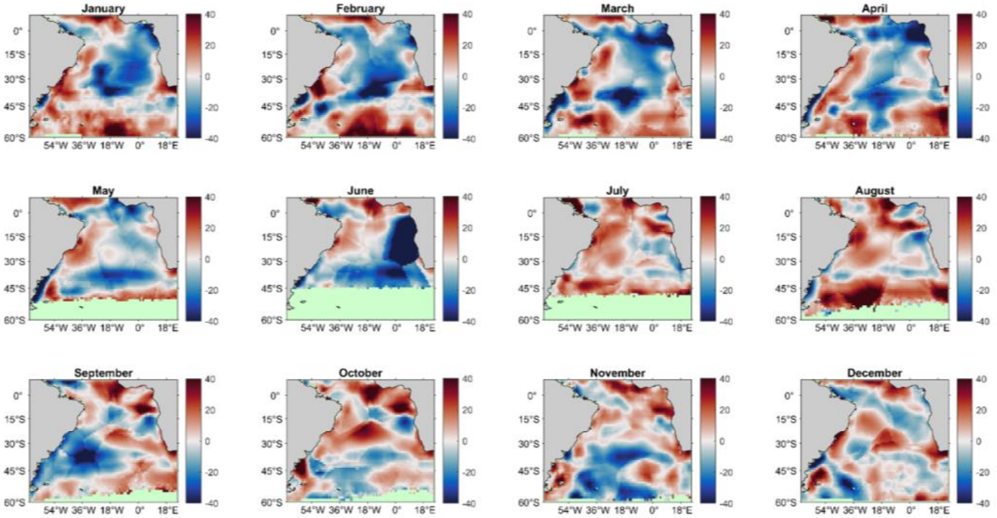

Fig. B2: Monthly comparison between *p*CO$_2$ $_{(sw)}$ climatology estimated by the SA-FNN$_{NCP}$ and Woolf et al (2019) climatology referenced to 2010 (SA-FNN$_{NCP}$ *p*CO$_2$ – Woolf *p*CO$_2$). Red (Blue) shades indicate regions where SA-FNN is greater (less) than the Woolf climatology.

Formatted: Font: Italic

Formatted: Font: Italic

Formatted: Font: Italic

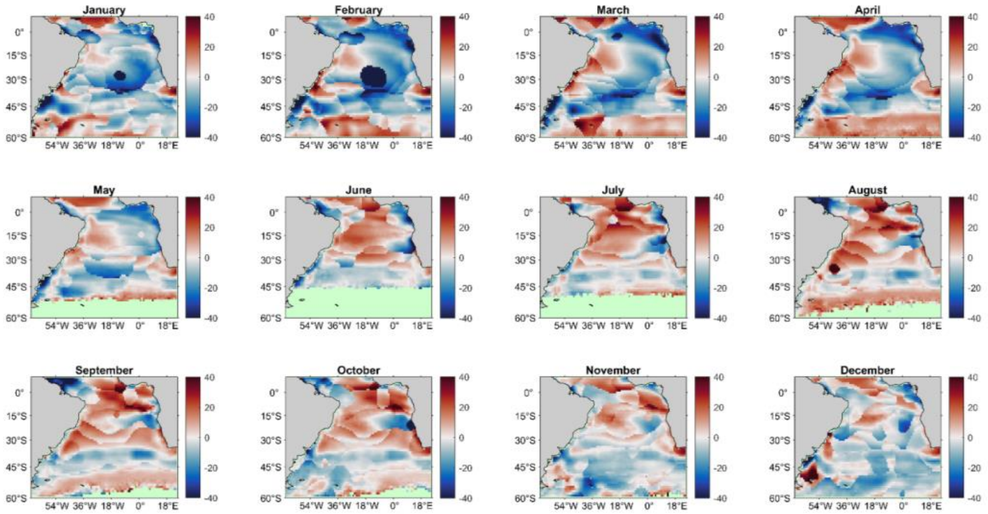

Fig. B3: Monthly comparison between $p\mathrm{CO}_{2\,(sw)}$ climatologies estimated by the SA-FNN$_{NCP}$ and W2020 (Watson et al, 2020a) climatology referenced to 2010 (SA-FNN$_{NCP}$ $p\mathrm{CO}_2$ – W2020 $p\mathrm{CO}_2$). Red (Blue) shades indicate regions where SA-FNN$_{NCP}$ is greater (less) than the W2020 climatology.

Formatted: Font: Italic

Formatted: Font: Italic

Formatted: Font: Italic

Appendix C – Biological parameter climatologies

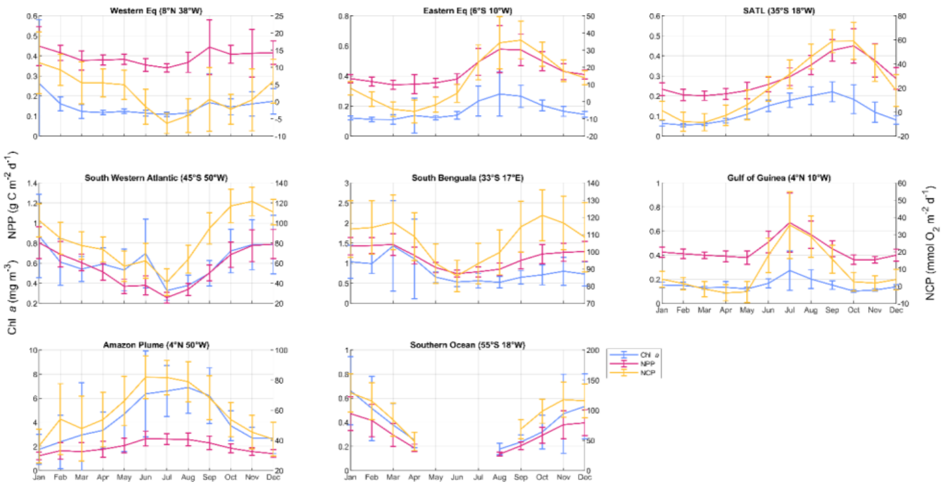

Fig. C1: Monthly climatologies of the biological parameters (Chl *a*, NPP and NCP) for the 8 stations (Fig. 1a). Chl *a* and NPP scale on the left axis, and NCP on the right. Note the different axis limits on each plot.

Data Availability

Moderate Resolution Imaging Spectroradiometer on Aqua (MODIS-A) estimates of chlorophyll-a, photosynthetically active radiation and sea surface temperature are available from the National Aeronautics Space Administration (NASA) ocean colour website (https://oceancolor.gsfc.nasa.gov/). Modelled sea surface salinity and mixed layer depth from the Copernicus Marine Environment Modelling Service global ocean physics reanalysis product (GLORYS12V1) are available from https://resources.marine.copernicus.eu/. ERA5 monthly reanalysis wind speeds are available from the Copernicus Climate Data Store (https://cds.climate.copernicus.eu/) $p\mathrm{CO}_{2\ (\mathrm{atm})}$ data are available from v5.5 of the global estimates of $p\mathrm{CO}_{2\ (\mathrm{sw})}$ dataset (Landschützer et al., 2016, 2017). *In situ* observations of $f\mathrm{CO}_{2\ (\mathrm{sw})}$ from v2020 of the Surface Ocean Carbon Atlas (SOCAT) are available from https://www.socat.info/index.php/data-access/. *In situ* Atlantic Meridional Transect data can be obtained from the British Oceanographic Data Centre (https://www.bodc.ac.uk/). $p\mathrm{CO}_{2\ (\mathrm{sw})}$ estimates from the W2020 are available from Watson et al. (2020a~~b~~). $p\mathrm{CO}_{2\ (\mathrm{sw})}$ estimates generated by the SA-FNN$_{\mathrm{NCP}}$, SA-FNN$_{\mathrm{NPP}}$, SA-FNN$_{\mathrm{CHLA}}$ and SA-

Formatted: Caption

Formatted: Font: Italic

Formatted: Font: Italic

Formatted: Font: Italic

Formatted: Font: Italic

Formatted: Font: Italic

Formatted: Font: Italic

Formatted: Font: Italic

FNN$_{\text{NO-BIO-2}}$ and SA-FNN$_{\text{NO-BIO-1}}$ are available from Pangaea (https://doi.pangaea.de/10.1594/PANGAEA.935936 ; ~~(~~Ford et al., ~~submitted~~2021a).

Author Contribution

DF, GT, JS and VK conceived and directed the research. DF developed the code and prepared the manuscript. GT, JS and VK provided comments that shaped the final manuscript.

Competing Interests

The authors declare that they have no conflict of interest.

Acknowledgements

DF was supported by a NERC GW4+ Doctoral Training Partnership studentship from the UK Natural Environment Research Council (NERC; NE/L002434/1). GT and VK were supported by the AMT4OceanSatFlux (4000125730/18/NL/FF/gp) contract from the European Space Agency and NERC National Capability funding to Plymouth Marine Laboratory for the Atlantic Meridional Transect (CLASS-AMT).
We would like to thank the captain and crew of *RRS Discovery*, *RRS James Clark Ross* and *RRS James Cook* for conducting the Atlantic Meridional Transects (AMT). We also thank the Natural Environment Research Council Earth Observation Data Acquisition and Analysis Service (NEODAAS) for use of the Linux cluster to process the MODIS-A satellite imagery. The Surface Ocean CO_2 Atlas (SOCAT) is an international effort, endorsed by the International Ocean Carbon Coordination Project (IOCCP), the Surface Ocean Lower Atmosphere Study (SOLAS) and the Integrated Marine Biosphere Research (IMBeR) program, to deliver a uniformly quality-controlled surface ocean CO_2 database. The many researchers and funding agencies responsible for the collection of data and quality control are thanked for their contributions to SOCAT. The AMT is funded by NERC through its National Capability Long-term Single Centre Science Programme, Climate Linked Atlantic Sector Science (NE/R015953/1). This study contributes to the international IMBeR project and is contribution number 366 of the AMT programme. We thank Jonathan Sharp and an anonymous reviewer for their valuable comments that improved the final manuscript.

References

Amari, S. I., Murata, N., Müller, K. R., Finke, M. and Yang, H. H.: Asymptotic statistical theory of overtraining and cross-validation, IEEE Trans. Neural Networks, 8(5), 985–996, doi:10.1109/72.623200, 1997.

Arnone, V., González-Dávila, M. and Magdalena Santana-Casiano, J.: CO_2 fluxes in the South African coastal region, Mar. Chem., 195(July), 41–49, doi:10.1016/j.marchem.2017.07.008, 2017.

Bakker, D. C. E., Pfeil, B., Landa, C. S., Metzl, N., O'Brien, K. M., Olsen, A., Smith, K., Cosca, C., Harasawa, S., Jones, S. D., Nakaoka, S. I., Nojiri, Y., Schuster, U., Steinhoff, T., Sweeney, C., Takahashi, T., Tilbrook, B., Wada, C., Wanninkhof, R., Alin, S. R., Balestrini, C. F., Barbero, L., Bates, N. R., Bianchi, A. A., Bonou, F., Boutin, J., Bozec, Y., Burger, E. F., Cai, W. J., Castle, R. D., Chen, L., Chierici, M., Currie, K., Evans, W., Featherstone, C., Feely, R. A., Fransson, A., Goyet, C., Greenwood, N., Gregor, L., Hankin, S., Hardman-Mountford, N. J., Harlay, J., Hauck, J., Hoppema, M., Humphreys, M. P., Hunt, C. W., Huss, B., Ibánhez, J. S. P., Johannessen, T., Keeling, R., Kitidis, V., Körtzinger, A., Kozyr, A., Krasakopoulou, E., Kuwata, A., Landschützer, P., Lauvset, S. K., Lefèvre, N., Lo Monaco, C., Manke, A., Mathis, J. T., Merlivat, L., Millero, F. J., Monteiro, P. M. S., Munro, D. R., Murata, A., Newberger, T., Omar, A. M., Ono, T., Paterson, K., Pearce, D., Pierrot, D., Robbins, L. L., Saito, S., Salisbury, J., Schlitzer, R., Schneider, B., Schweitzer, R., Sieger, R., Skjelvan, I., Sullivan, K. F., Sutherland, S. C., Sutton, A. J., Tadokoro, K., Telszewski, M., Tuma, M., Van Heuven, S. M. A. C., Vandemark, D., Ward, B., Watson, A. J. and Xu, S.: A multi-decade record of high-quality fCO_2 data in version 3 of the Surface Ocean CO_2 Atlas (SOCAT), Earth Syst. Sci. Data, 8(2), 383–413, doi:10.5194/essd-8-383-2016, 2016.

Banks, A. C., Vendt, R., Alikas, K., Bialek, A., Kuusk, J., Lerebourg, C., Ruddick, K., Tilstone, G., Vabson, V., Donlon, C. and Casal, T.: Fiducial reference measurements for satellite ocean colour (FRM4SOC), Remote Sens., 12(8), doi:10.3390/RS12081322, 2020.

Behrenfeld, M. J. and Falkowski, P. G.: Photosynthetic rates derived from satellite-based chlorophyll concentration, Limnol. Oceanogr., 42(1), 1–20, doi:10.4319/lo.1997.42.1.0001, 1997.

Behrenfeld, M. J., O'Malley, R. T., Boss, E. S., Westberry, T. K., Graff, J. R., Halsey, K. H., Milligan, A. J., Siegel, D. A. and Brown, M. B.: Revaluating ocean warming impacts on global phytoplankton, Nat. Clim. Chang., 6(3), 323–330, doi:10.1038/nclimate2838, 2016.

Benallal, M. A., Moussa, H., Lencina-Avila, J. M., Touratier, F., Goyet, C., El Jai, M. C., Poisson, N. and Poisson, A.: Satellite-derived CO_2 flux in the surface seawater of the Austral Ocean south of Australia, Int. J. Remote Sens., 38(6), 1600–1625, doi:10.1080/01431161.2017.1286054, 2017.

BIPM: Evaluation of measurement data—Guide to the expression of uncertainty in measurement. [online] Available from: http://www.bipm.org/utils/common/documents/jcgm/JCGM_100_2008_E.pdf, 2008.

Bourlès, B., Lumpkin, R., McPhaden, M. J., Hernandez, F., Nobre, P., Campos, E., Yu, L., Planton, S., Busalacchi, A., Moura, A. D., Servain, J. and Trotte, J.: THE PIRATA PROGRAM, Bull. Am. Meteorol. Soc., 89(8), 1111–1126, doi:10.1175/2008BAMS2462.1, 2008.

Brewin, R. J. W., Dall'Olmo, G., Pardo, S., van Dongen-Vogels, V. and Boss, E. S.: Underway spectrophotometry along the Atlantic Meridional Transect reveals high performance in satellite chlorophyll retrievals, Remote Sens. Environ., doi:10.1016/j.rse.2016.05.005, 2016.

Bruto, L., Araujo, M., Noriega, C., Veleda, D. and Lefèvre, N.: Variability of CO_2 fugacity at the western edge of the tropical Atlantic Ocean from the 8°N to 38°W PIRATA buoy, Dyn. Atmos. Ocean., 78, 1–13, doi:10.1016/j.dynatmoce.2017.01.003, 2017.

Chen, C. T. A., Huang, T. H., Fu, Y. H., Bai, Y. and He, X.: Strong sources of CO_2 in upper estuaries become sinks of CO_2 in large river plumes, Curr. Opin. Environ. Sustain., 4(2), 179–185, doi:10.1016/j.cosust.2012.02.003, 2012.

Chierici, M., Signorini, S. R., Mattsdotter-Björk, M., Fransson, A. and Olsen, A.: Surface water fCO_2 algorithms for the high-latitude Pacific sector of the Southern Ocean, Remote Sens. Environ., 119, 184–196, doi:10.1016/j.rse.2011.12.020, 2012.

Coles, V. J., Brooks, M. T., Hopkins, J., Stukel, M. R., Yager, P. L. and Hood, R. R.: The pathways and properties of the Amazon river plume in the tropical North Atlantic Ocean, J. Geophys. Res. Ocean., 118(12), 6894–6913, doi:10.1002/2013JC008981, 2013.

Cooley, S. R., Coles, V. J., Subramaniam, A. and Yager, P. L.: Seasonal variations in the Amazon plume-related atmospheric carbon sink, Global Biogeochem. Cycles, 21(3), 1–15, doi:10.1029/2006GB002831, 2007.

Dai, A. and Trenberth, K. E.: Estimates of freshwater discharge from continents: Latitudinal and seasonal variations, J. Hydrometeorol., 3(6), 660–687, doi:10.1175/1525-7541(2002)003<0660:EOFDFC>2.0.CO;2, 2002.

Demuth, H., Beale, M. and Hagan, M.: Neural Network Toolbox 6 Users Guide, 3 Apple Hill Drive, Natick, MA., 2008.

DeVries, T.: The oceanic anthropogenic CO2 sink: Storage, air-sea fluxes, and transports over the industrial era, Global

Biogeochem. Cycles, 28(7), 631–647, doi:10.1002/2013GB004739, 2014.

Dickson, A. G., Sabine, C. L. and Christian, J. R.: Guide to Best Practices for Ocean CO_2 measurements., 2007.

Dogliotti, A. I., Lutz, V. A. and Segura, V.: Estimation of primary production in the southern Argentine continental shelf and shelf-break regions using field and remote sensing data, Remote Sens. Environ., 140, 497–508, doi:10.1016/j.rse.2013.09.021, 2014.

Donlon, C. J., Nightingale, T. J., Sheasby, T., Turner, J., Robinson, I. S. and Emergy, W. J.: Implications of the oceanic thermal skin temperature deviation at high wind speed, Geophys. Res. Lett., 26(16), 2505–2508, doi:10.1029/1999GL900547, 1999.

Duarte, C. M., Regaudie-de-Gioux, A., Arrieta, J. M., Delgado-Huertas, A. and Agustí, S.: The Oligotrophic Ocean Is Heterotrophic, Ann. Rev. Mar. Sci., 5(1), 551–569, doi:10.1146/annurev-marine-121211-172337, 2013.

Ducklow, H. W. and Doney, S. C.: What Is the Metabolic State of the Oligotrophic Ocean? A Debate, Ann. Rev. Mar. Sci., 5(1), 525–533, doi:10.1146/annurev-marine-121211-172331, 2013.

Fay, A. R. and McKinley, G. A.: Global trends in surface ocean pCO_2 from in situ data, Global Biogeochem. Cycles, 27(2), 541–557, doi:10.1002/gbc.20051, 2013.

Ford, D., Tilstone, G. H., Shutler, J. D. and Kitidis, V.: Interpolated surface ocean carbon dioxide partial pressure for the South Atlantic Ocean (2002-2018) using different biological parameters, PANGAEA, doi:10.1594/PANGAEA.935936, 2021a.

Ford, D., Tilstone, G. H., Shutler, J. D., Kitidis, V., Lobanova, P., Schwarz, J., Poulton, A. J., Serret, P., Lamont, T., Chuqui, M., Barlow, R., Lozano, J., Kampel, M. and Brandini, F.: Wind speed and mesoscale features drive net autotrophy in the South Atlantic Ocean, Remote Sens. Environ., 260, 112435, doi:10.1016/j.rse.2021.112435, 2021b.

Friedlingstein, P., O'Sullivan, M., Jones, M. W., Andrew, R. M., Hauck, J., Olsen, A., Peters, G. P., Peters, W., Pongratz, J., Sitch, S., Le Quéré, C., Canadell, J. G., Ciais, P., Jackson, R. B., Alin, S., Aragão, L. E. O. C., Arneth, A., Arora, V., Bates, N. R., Becker, M., Benoit-Cattin, A., Bittig, H. C., Bopp, L., Bultan, S., Chandra, N., Chevallier, F., Chini, L. P., Evans, W., Florentie, L., Forster, P. M., Gasser, T., Gehlen, M., Gilfillan, D., Gkritzalis, T., Gregor, L., Gruber, N., Harris, I., Hartung, K., Haverd, V., Houghton, R. A., Ilyina, T., Jain, A. K., Joetzjer, E., Kadono, K., Kato, E., Kitidis, V., Korsbakken, J. I., Landschützer, P., Lefèvre, N., Lenton, A., Lienert, S., Liu, Z., Lombardozzi, D., Marland, G., Metzl, N., Munro, D. R., Nabel, J. E. M. S., Nakaoka, S.-I., Niwa, Y., O'Brien, K., Ono, T., Palmer, P. I., Pierrot, D., Poulter, B., Resplandy, L., Robertson, E., Rödenbeck, C., Schwinger, J., Séférian, R., Skjelvan, I., Smith, A. J. P., Sutton, A. J., Tanhua, T., Tans, P. P., Tian, H., Tilbrook, B., van der Werf, G., Vuichard, N., Walker, A. P., Wanninkhof, R., Watson, A. J., Willis, D., Wiltshire, A. J., Yuan, W., Yue, X. and Zaehle, S.: Global Carbon Budget 2020, Earth Syst. Sci. Data, 12(4), 3269–3340, doi:10.5194/essd-12-3269-2020, 2020.

Gist, N., Serret, P., Woodward, E. M. S., Chamberlain, K. and Robinson, C.: Seasonal and spatial variability in plankton production and respiration in the Subtropical Gyres of the Atlantic Ocean, Deep. Res. Part II Top. Stud. Oceanogr., 56(15), 931–940, doi:10.1016/j.dsr2.2008.10.035, 2009.

Goddijn-Murphy, L. M., Woolf, D. K., Land, P. E., Shutler, J. D. and Donlon, C.: The OceanFlux Greenhouse Gases methodology for deriving a sea surface climatology of CO_2 fugacity in support of air-sea gas flux studies, Ocean Sci., 11(4), 519–541, doi:10.5194/os-11-519-2015, 2015.

González-Dávila, M., Santana-Casiano, J. M. and Ucha, I. R.: Seasonal variability of fCO_2 in the Angola-Benguela region, Prog. Oceanogr., 83(1–4), 124–133, doi:10.1016/j.pocean.2009.07.033, 2009.

Gregor, L. and Monteiro, P. M. S.: Is the southern benguela a significant regional sink of CO_2?, S. Afr. J. Sci., 109(5–6), 1–5, doi:10.1590/sajs.2013/20120094, 2013.

Holding, T., Ashton, I. G., Shutler, J. D., Land, P. E., Nightingale, P. D., Rees, A. P., Brown, I., Piolle, J.-F., Kock, A., Bange, H. W., Woolf, D. K., Goddijn-Murphy, L., Pereira, R., Paul, F., Girard-Ardhuin, F., Chapron, B., Rehder, G., Ardhuin, F. and Donlon, C. J.: The FluxEngine air–sea gas flux toolbox: simplified interface and extensions for in situ analyses and multiple sparingly soluble gases, Ocean Sci., 15(6), 1707–1728, doi:10.5194/os-15-1707-2019, 2019.

Hu, C., Lee, Z. and Franz, B.: Chlorophyll a algorithms for oligotrophic oceans: A novel approach based on three-band reflectance difference, J. Geophys. Res. Ocean., 117(1), 1–25, doi:10.1029/2011JC007395, 2012.

Hutchings, L., van der Lingen, C. D., Shannon, L. J., Crawford, R. J. M., Verheye, H. M. S., Bartholomae, C. H., van der Plas, A. K., Louw, D., Kreiner, A., Ostrowski, M., Fidel, Q., Barlow, R. G., Lamont, T., Coetzee, J., Shillington, F., Veitch, J., Currie, J. C. and Monteiro, P. M. S.: The Benguela Current: An ecosystem of four components, Prog. Oceanogr., 83(1–4), 15–32, doi:10.1016/j.pocean.2009.07.046, 2009.

Ibánhez, J. S. P., Diverrès, D., Araujo, M. and Lefèvre, N.: Seasonal and interannual variability of sea-air CO_2 fluxes in the tropical Atlantic affected by the Amazon River plume, Global Biogeochem. Cycles, 29(10), 1640–1655, doi:10.1002/2015GB005110, 2015.

IPCC: Climate Change 2013: The Physical Science Basis. Contribution of Working Group I to the Fifth Assessment Report of the Intergovernmental Panel on Climate Change, edited by T. F. Stocker, D. Qin, G.-K. Plattner, M. B. Tignor, S. K. Allen, J. Boschung, A. Nauels, Y. Xia, V. Bex, and P. M. Midgley, Cambridge University Press, Cambridge, UK., 2013.

Jiang, Z. P., Cai, W. J., Lehrter, J., Chen, B., Ouyang, Z., Le, C., Roberts, B. J., Hussain, N., Scaboo, M. K., Zhang, J. and Xu, Y.: Spring net community production and its coupling with the CO_2 dynamics in the surface water of the northern Gulf of Mexico, Biogeosciences, 16(18), 3507–3525, doi:10.5194/bg-16-3507-2019, 2019.

Kaiser, J., Reuer, M. K., Barnett, B. and Bender, M. L.: Marine productivity estimates from continuous O_2/Ar ratio measurements by membrane inlet mass spectrometry, Geophys. Res. Lett., 32(19), n/a-n/a, doi:10.1029/2005GL023459, 2005.

Kitidis, V., Tilstone, G. H., Serret, P., Smyth, T. J., Torres, R. and Robinson, C.: Oxygen photolysis in the Mauritanian upwelling: Implications for net community production, Limnol. Oceanogr., 59(2), 299–310, doi:10.4319/lo.2014.59.2.0299, 2014.

Kitidis, V., Brown, I., Hardman-mountford, N. and Lefèvre, N.: Surface ocean carbon dioxide during the Atlantic Meridional Transect (1995 – 2013); evidence of ocean acidification, Prog. Oceanogr., 158, 65–75, doi:10.1016/j.pocean.2016.08.005, 2017.

Koffi, U., Lefèvre, N., Kouadio, G. and Boutin, J.: Surface CO_2 parameters and air-sea CO_2 flux distribution in the eastern equatorial Atlantic Ocean, J. Mar. Syst., 82(3), 135–144, doi:10.1016/j.jmarsys.2010.04.010, 2010.

Koffi, U., Kouadio, G. and Kouadio, Y. K.: Estimates and Variability of the Air-Sea CO_2 Fluxes in the Gulf of Guinea during the 2005-2007 Period, Open J. Mar. Sci., 06(01), 11–22, doi:10.4236/ojms.2016.61002, 2016.

Kroopnick, P.: Isotopic fractionations during oxygen consumption and carbonate dissolution within the North Atlantic Deep Water, Earth Planet. Sci. Lett., 49(2), 485–498, doi:10.1016/0012-821X(80)90089-8, 1980.

Kulk, G., Platt, T., Dingle, J., Jackson, T., Jönsson, B. F., Bouman, H. A., Babin, M., Brewin, R. J. W., Doblin, M., Estrada, M., Figueiras, F. G., Furuya, K., González-Benítez, N., Gudfinnsson, H. G., Gudmundsson, K., Huang, B., Isada, T., Kovač, Ž., Lutz, V. A., Marañón, E., Raman, M., Richardson, K., Rozema, P. D., van de Poll, W. H., Segura, V., Tilstone, G. H., Uitz, J., van Dongen-Vogels, V., Yoshikawa, T. and Sathyendranath, S.: Primary production, an index of climate change in the ocean: Satellite-based estimates over two decades, Remote Sens., 12(5), doi:10.3390/rs12050826, 2020.

Lamont, T., Barlow, R. G. and Kyewalyanga, M. S.: Physical drivers of phytoplankton production in the southern Benguela upwelling system, Deep. Res. Part I Oceanogr. Res. Pap., 90(1), 1–16, doi:10.1016/j.dsr.2014.03.003, 2014.

Landschützer, P., Gruber, N., Bakker, D. C. E., Schuster, U., Nakaoka, S., Payne, M. R., Sasse, T. P. and Zeng, J.: A neural network-based estimate of the seasonal to inter-annual variability of the Atlantic Ocean carbon sink, Biogeosciences, 10(11), 7793–7815, doi:10.5194/bg-10-7793-2013, 2013.

Landschützer, P., Gruber, N., Bakker, D. C. E. and Schuster, U.: Recent variability of the global ocean carbon sink, Global Biogeochem. Cycles, 28(9), 927–949, doi:10.1002/2014GB004853, 2014.

Landschützer, P., Gruber, N. and Bakker, D. C. E.: Decadal variations and trends of the global ocean carbon sink, Global Biogeochem. Cycles, 30(10), 1396–1417, doi:10.1002/2015GB005359, 2016.

Landschützer, P., Gruber, N. and Bakker, D. C. E.: An observation-based global monthly gridded sea surface pCO_2 product from 1982 onward and its monthly climatology (NCEI Accession 0160558), NOAA Natl. Centers Environ. Information. Dataset, doi:10.7289/v5z899n6, 2017.

Landschützer, P., Laruelle, G. G., Roobaert, A. and Regnier, P.: A uniform pCO_2 climatology combining open and coastal oceans, Earth Syst. Sci. Data, 12(4), 2537–2553, doi:10.5194/essd-12-2537-2020, 2020.

Laruelle, G. G., Lauerwald, R., Pfeil, B. and Regnier, P.: Regionalized global budget of the CO_2 exchange at the air-water interface in continental shelf seas, Global Biogeochem. Cycles, 28(11), 1199–1214, doi:10.1002/2014GB004832, 2014.

Lavender, S. J., Pinkerton, M. H., Froidefond, J.-M., Morales, J., Aiken, J. and Moore, G. F.: SeaWiFS validation in European coastal waters using optical and bio-geochemical measurements, Int. J. Remote Sens., 25(7–8), 1481–1488, doi:10.1080/01431160310001592481, 2004.

Lee, Z., Marra, J., Perry, M. J. and Kahru, M.: Estimating oceanic primary productivity from ocean color remote sensing: A strategic assessment, J. Mar. Syst., 149, 50–59, doi:10.1016/j.jmarsys.2014.11.015, 2015.

Lefèvre, N., Guillot, A., Beaumont, L. and Danguy, T.: Variability of fCO_2 in the Eastern Tropical Atlantic from a moored buoy, J. Geophys. Res. Ocean., 113(1), doi:10.1029/2007JC004146, 2008.

Lefèvre, N., Veleda, D., Araujo, M. and Caniaux, G.: Variability and trends of carbon parameters at a time series in the eastern tropical Atlantic, Tellus, Ser. B Chem. Phys. Meteorol., 68(1), doi:10.3402/tellusb.v68.30305, 2016.

Lefèvre, N., Montes, M. F., Gaspar, F. L., Rocha, C., Jiang, S., De Araújo, M. C. and Severino Pino Ibánhez, J.: Net heterotrophy in the Amazon continental shelf changes rapidly to a sink of CO_2 in the outer Amazon plume, Front. Mar. Sci., 4(SEP), 1–16, doi:10.3389/fmars.2017.00278, 2017.

Lefèvre, N., Tyaquiçã, P., Veleda, D., Perruche, C. and van Gennip, S. J.: Amazon River propagation evidenced by a CO_2 decrease at 8°N, 38°W in September 2013, J. Mar. Syst., 211(July), 103419, doi:10.1016/j.jmarsys.2020.103419, 2020.

Lencina-Avila, J. M., Ito, R. G., Garcia, C. A. E. and Tavano, V. M.: Sea-air carbon dioxide fluxes along 35°S in the South Atlantic Ocean, Deep. Res. Part I Oceanogr. Res. Pap., 115, 175–187, doi:10.1016/j.dsr.2016.06.004, 2016.

Liu, W. T. and Xie, X.: Space Observation of Carbon Dioxide Partial Pressure at Ocean Surface, IEEE J. Sel. Top. Appl. Earth Obs. Remote Sens., 10(12), 5472–5484, doi:10.1109/JSTARS.2017.2766138, 2017.

Longhurst, A.: Ecological geography of the sea, Academic Press, San Diego., 1998.

Longhurst, A., Sathyendranath, S., Platt, T. and Caverhill, C.: An estimate of global primary production in the ocean from satellite radiometer data, J. Plankton Res., 17(6), 1245–1271, doi:10.1093/plankt/17.6.1245, 1995.

Luz, B. and Barkan, E.: Assessment of Oceanic Productivity with the Triple-Isotope Composition of Dissolved Oxygen, Science (80-.)., 288(5473), 2028–2031, doi:10.1126/science.288.5473.2028, 2000.

Marañón, E., Behrenfeld, M. J., González, N., Mouriño, B. and Zubkov, M. V.: High variability of primary production in oligotrophic waters of the Atlantic Ocean: Uncoupling from phytoplankton biomass and size structure, Mar. Ecol. Prog. Ser., 257, 1–11, doi:10.3354/meps257001, 2003.

Morel, A.: Light and marine photosynthesis: a spectral model with geochemical and climatological implications, Prog. Oceanogr., 26(3), 263–306, doi:10.1016/0079-6611(91)90004-6, 1991.

Moussa, H., Benallal, M. A., Goyet, C. and Lefèvre, N.: Satellite-derived CO_2 fugacity in surface seawater of the tropical Atlantic Ocean using a feedforward neural network, Int. J. Remote Sens., 37(3), 580–598, doi:10.1080/01431161.2015.1131872, 2016.

Nightingale, P. D., Malin, G., Law, C. S., Watson, A. J., Liss, P. S., Liddicoat, M. I., Boutin, J. and Upstill-Goddard, R. C.: In situ evaluation of air-sea gas exchange parameterizations using novel conservative and volatile tracers, Global Biogeochem. Cycles, 14(1), 373–387, doi:10.1029/1999GB900091, 2000.

O'Reilly, J. E. and Werdell, P. J.: Chlorophyll algorithms for ocean color sensors - OC4, OC5 & OC6, Remote Sens. Environ., 229(May), 32–47, doi:10.1016/j.rse.2019.04.021, 2019.

O'Reilly, J. E., Maritorena, S., Mitchell, B. G., Siegel, D. A., Carder, K. L., Garver, S. A., Kahru, M. and Mcclain, C.: Ocean color chlorophyll algorithms for SeaWiFS encompassing chlorophyll concentrations between, J. Geophys. Res., 103(C11), 24937–24953, 1998.

Parard, G., Lefévre, N. and Boutin, J.: Sea water fugacity of CO_2 at the PIRATA mooring at 6°S, 10°W, Tellus, Ser. B Chem. Phys. Meteorol., 62(5), 636–648, doi:10.1111/j.1600-0889.2010.00503.x, 2010.

Pfeil, B., Olsen, A., Bakker, D. C. E., Hankin, S., Koyuk, H., Kozyr, A., Malczyk, J., Manke, A., Metzl, N., Sabine, C. L., Akl, J., Alin, S. R., Bates, N., Bellerby, R. G. J., Borges, A., Boutin, J., Brown, P. J., Cai, W. J., Chavez, F. P., Chen, A., Cosca, C., Fassbender, A. J., Feely, R. A., González-Dávila, M., Goyet, C., Hales, B., Hardman-Mountford, N., Heinze, C., Hood, M., Hoppema, M., Hunt, C. W., Hydes, D., Ishii, M., Johannessen, T., Jones, S. D., Key, R. M., Körtzinger, A., Landschützer, P., Lauvset, S. K., Lefèvre, N., Lenton, A., Lourantou, A., Merlivat, L., Midorikawa, T., Mintrop, L., Miyazaki, C., Murata, A., Nakadate, A., Nakano, Y., Nakaoka, S., Nojiri, Y., Omar, A. M., Padin, X. A., Park, G. H., Paterson, K., Perez, F. F., Pierrot, D., Poisson, A., Ríos, A. F., Santana-Casiano, J. M., Salisbury, J., Sarma, V. V. S. S., Schlitzer, R., Schneider, B., Schuster, U., Sieger, R., Skjelvan, I., Steinhoff, T., Suzuki, T., Takahashi, T., Tedesco, K., Telszewski, M., Thomas, H., Tilbrook, B., Tjiputra, J., Vandemark, D., Veness, T., Wanninkhof, R., Watson, A. J., Weiss, R., Wong, C. S. and Yoshikawa-Inoue, H.: A uniform, quality controlled Surface Ocean CO_2 Atlas (SOCAT), Earth Syst. Sci. Data, 5(1), 125–143, doi:10.5194/essd-5-125-2013, 2013.

Poulton, A. J., Holligan, P. M., Hickman, A., Kim, Y. N., Adey, T. R., Stinchcombe, M. C., Holeton, C., Root, S. and Woodward, E. M. S.: Phytoplankton carbon fixation, chlorophyll-biomass and diagnostic pigments in the Atlantic Ocean, Deep. Res. Part II Top. Stud. Oceanogr., 53(14–16), 1593–1610, doi:10.1016/j.dsr2.2006.05.007, 2006.

Raven, J., Caldeira, K., Elderfield, H., Hoegh-Guldberg, O., Liss, P., Riebesell, U., Shepherd, J., Turley, C. and Watson, A.: Ocean acidification due to increasing atmospheric carbon dioxide, The Royal Society, London., 2005.

Reynolds, R. W., Rayner, N. A., Smith, T. M., Stokes, D. C. and Wang, W.: An improved in situ and satellite SST analysis for climate, J. Clim., 15(13), 1609–1625, doi:10.1175/1520-0442(2002)015<1609:AIISAS>2.0.CO;2, 2002.

Rödenbeck, C., Bakker, D. C. E., Gruber, N., Iida, Y., Jacobson, A. R., Jones, S., Landschützer, P., Metzl, N., Nakaoka, S., Olsen, A., Park, G.-H., Peylin, P., Rodgers, K. B., Sasse, T. P., Schuster, U., Shutler, J. D., Valsala, V., Wanninkhof, R. and Zeng, J.: Data-based estimates of the ocean carbon sink variability – first results of the Surface Ocean pCO$_2$ Mapping intercomparison (SOCOM), Biogeosciences, 12(23), 7251–7278, doi:10.5194/bg-12-7251-2015, 2015.

Saba, V. S., Friedrichs, M. A. M., Antoine, D., Armstrong, R. A., Asanuma, I., Behrenfeld, M. J., Ciotti, A. M., Dowell, M., Hoepffner, N., Hyde, K. J. W., Ishizaka, J., Kameda, T., Marra, J., Mélin, F., Morel, A., O'reilly, J., Scardi, M., Smith, W. O., Smyth, T. J., Tang, S., Uitz, J., Waters, K. and Westberry, T. K.: An evaluation of ocean color model estimates of marine primary productivity in coastal and pelagic regions across the globe, Biogeosciences, 8, 489–503, doi:10.5194/bg-8-489-2011, 2011.

Sabine, C. L., Hankin, S., Koyuk, H., Bakker, D. C. E., Pfeil, B., Olsen, A., Metzl, N., Kozyr, A., Fassbender, A., Manke, A., Malczyk, J., Akl, J., Alin, S. R., Bellerby, R. G. J., Borges, A., Boutin, J., Brown, P. J., Cai, W. J., Chavez, F. P., Chen, A., Cosca, C., Feely, R. A., González-Dávila, M., Goyet, C., Hardman-Mountford, N., Heinze, C., Hoppema, M., Hunt, C. W., Hydes, D., Ishii, M., Johannessen, T., Key, R. M., Körtzinger, A., Landschützer, P., Lauvset, S. K., Lefèvre, N., Lenton, A., Lourantou, A., Merlivat, L., Midorikawa, T., Mintrop, L., Miyazaki, C., Murata, A., Nakadate, A., Nakano, Y., Nakaoka, S., Nojiri, Y., Omar, A. M., Padin, X. A., Park, G. H., Paterson, K., Perez, F. F., Pierrot, D., Poisson, A., Ríos, A. F., Salisbury, J., Santana-Casiano, J. M., S. Sarma, V. V. S., Schlitzer, R., Schneider, B., Schuster, U., Sieger, R., Skjelvan, I., Steinhoff, T., Suzuki, T., Takahashi, T., Tedesco, K., Telszewski, M., Thomas, H., Tilbrook, B., Vandemark, D., Veness, T., Watson, A. J., Weiss, R., Wong, C. S. and Yoshikawa-Inoue, H.: Surface Ocean CO$_2$ Atlas (SOCAT) gridded data products, Earth Syst. Sci. Data, 5(1), 145–153, doi:10.5194/essd-5-145-2013, 2013.

Santana-Casiano, J. M., González-Dávila, M. and Ucha, I. R.: Carbon dioxide fluxes in the Benguela upwelling system during winter and spring: A comparison between 2005 and 2006, Deep Sea Res. Part II Top. Stud. Oceanogr., 56(8–10), 533–541, doi:10.1016/j.dsr2.2008.12.010, 2009.

Sathyendranath, S., Platt, T., Kovač, Ž., Dingle, J., Jackson, T., Brewin, R. J. W., Franks, P., Marañón, E., Kulk, G. and Bouman, H. A.: Reconciling models of primary production and photoacclimation [Invited], Appl. Opt., 59(10), C100, doi:10.1364/AO.386252, 2020.

Schloss, I. R., Ferreyra, G. A., Ferrario, M. E., Almandoz, G. O., Codina, R., Bianchi, A. A., Balestrini, C. F., Ochoa, H. A., Pino, D. R. and Poisson, A.: Role of plankton communities in sea-air variations in pCO$_2$ in the SW Atlantic Ocean, Mar. Ecol. Prog. Ser., 332, 93–106, doi:10.3354/meps332093, 2007.

Serret, P., Robinson, C., Aranguren-Gassis, M., García-Martín, E. E., Gist, N., Kitidis, V., Lozano, J., Stephens, J., Harris, C. and Thomas, R.: Both respiration and photosynthesis determine the scaling of plankton metabolism in the oligotrophic ocean, Nat. Commun., 6, 1–10, doi:10.1038/ncomms7961, 2015.

Shutler, J. D., Land, P. E., Piolle, J. F., Woolf, D. K., Goddijn-Murphy, L., Paul, F., Girard-Ardhuin, F., Chapron, B. and Donlon, C. J.: FluxEngine: A flexible processing system for calculating atmosphere-ocean carbon dioxide gas fluxes and climatologies, J. Atmos. Ocean. Technol., 33(4), 741–756, doi:10.1175/JTECH-D-14-00204.1, 2016.

Shutler, J. D., Wanninkhof, R., Nightingale, P. D., Woolf, D. K., Bakker, D. C., Watson, A., Ashton, I., Holding, T., Chapron, B., Quilfen, Y., Fairall, C., Schuster, U., Nakajima, M. and Donlon, C. J.: Satellites will address critical science priorities for quantifying ocean carbon, Front. Ecol. Environ., 18(1), 27–35, doi:10.1002/fee.2129, 2020.

Smith, W. O. and Demaster, D. J.: Phytoplankton biomass and productivity in the Amazon River plume: Correlation with seasonal river discharge, Cont. Shelf Res., 16(3), 291–319, doi:10.1016/0278-4343(95)00007-N, 1996.

Smyth, T. J., Tilstone, G. H. and Groom, S. B.: Integration of radiative transfer into satellite models of ocean primary production, J. Geophys. Res. C Ocean., 110(10), 1–11, doi:10.1029/2004JC002784, 2005.

Stephens, M. P., Samuels, G., Olson, D. B., Fine, R. A. and Takahashi, T.: Sea-air flux of CO$_2$ in the North Pacific using shipboard and satellite data, J. Geophys. Res., 100(C7), 13571, doi:10.1029/95JC00901, 1995.

Takahashi, T., Sutherland, S. C., Wanninkhof, R., Sweeney, C., Feely, R. A., Chipman, D. W., Hales, B., Friederich, G., Chavez, F., Sabine, C., Watson, A., Bakker, D. C. E., Schuster, U., Metzl, N., Yoshikawa-Inoue, H., Ishii, M., Midorikawa, T., Nojiri, Y., Körtzinger, A., Steinhoff, T., Hoppema, M., Olafsson, J., Arnarson, T. S., Tilbrook, B., Johannessen, T., Olsen, A., Bellerby, R., Wong, C. S., Delille, B., Bates, N. R. and de Baar, H. J. W.: Climatological mean and decadal change in surface ocean pCO_2, and net sea-air CO_2 flux over the global oceans, Deep. Res. Part II Top. Stud. Oceanogr., 56(8–10), 554–577, doi:10.1016/j.dsr2.2008.12.009, 2009.

Taylor, J. R.: An introduction to error analysis, University Science Books, Sausalito, Calif., 1997.

Tilstone, G. H., Smyth, T. J., Gowen, R. J., Martinez-Vicente, V. and Groom, S. B.: Inherent optical properties of the Irish Sea and their effect on satellite primary production algorithms, J. Plankton Res., 27(11), 1127–1148, doi:10.1093/plankt/fbi075, 2005.

Tilstone, G. H., Smyth, T., Poulton, A. and Hutson, R.: Measured and remotely sensed estimates of primary production in the Atlantic Ocean from 1998 to 2005, Deep. Res. Part II Top. Stud. Oceanogr., 56(15), 918–930, doi:10.1016/j.dsr2.2008.10.034, 2009.

Tilstone, G. H., Xie, Y. yuan, Robinson, C., Serret, P., Raitsos, D. E., Powell, T., Aranguren-Gassis, M., Garcia-Martin, E. E. and Kitidis, V.: Satellite estimates of net community production indicate predominance of net autotrophy in the Atlantic Ocean, Remote Sens. Environ., 164, 254–269, doi:10.1016/j.rse.2015.03.017, 2015.

Tilstone, G. H., Lange, P. K., Misra, A., Brewin, R. J. W. and Cain, T.: Micro-phytoplankton photosynthesis, primary production and potential export production in the Atlantic Ocean, Prog. Oceanogr., 158, 109–129, doi:10.1016/j.pocean.2017.01.006, 2017.

Valerio, A. M., Kampel, M., Ward, N. D., Sawakuchi, H. O., Cunha, A. C. and Richey, J. E.: CO_2 partial pressure and fluxes in the Amazon River plume using in situ and remote sensing data, Cont. Shelf Res., 215(May 2020), 104348, doi:10.1016/j.csr.2021.104348, 2021.

Varona, H. L., Veleda, D., Silva, M., Cintra, M. and Araujo, M.: Amazon River plume influence on Western Tropical Atlantic dynamic variability, Dyn. Atmos. Ocean., 85(September 2018), 1–15, doi:10.1016/j.dynatmoce.2018.10.002, 2019.

Watson, A. J., Schuster, U., Shutler, J. D., Holding, T., Ashton, I. G. C., Landschützer, P., Woolf, D. K. and Goddijn-Murphy, L.: Interpolated Global surface ocean carbon dioxide partial pressure and ocean-atmosphere fluxes 1992-2018, corrected for surface temperature deviations, PANGAEA, doi:10.1594/PANGAEA.922985, 2020a.

Watson, A. J., Schuster, U., Shutler, J. D., Holding, T., Ashton, I. G. C., Landschützer, P., Woolf, D. K. and Goddijn-Murphy, L.: Revised estimates of ocean-atmosphere CO_2 flux are consistent with ocean carbon inventory, Nat. Commun., 11(1), 1–6, doi:10.1038/s41467-020-18203-3, 2020b.

Weiss, R. F.: Carbon dioxide in water and seawater: the solubility of a non-ideal gas, Mar. Chem., 2(3), 203–215, doi:10.1016/0304-4203(74)90015-2, 1974.

Williams, P. J. le B., Quay, P. D., Westberry, T. K. and Behrenfeld, M. J.: The Oligotrophic Ocean Is Autotrophic, Ann. Rev. Mar. Sci., 5(1), 535–549, doi:10.1146/annurev-marine-121211-172335, 2013.

Woolf, D. K., Land, P. E., Shutler, J. D., Goddijn-Murphy, L. M. and Donlon, C. J.: On the calculation of air-sea fluxes of CO_2 in the presence of temperature and salinity gradients, J. Geophys. Res. Ocean., 121(2), 1229–1248, doi:10.1002/2015JC011427, 2016.

Woolf, D. K., Shutler, J. D., Goddijn-Murphy, L., Watson, A. J., Chapron, B., Nightingale, P. D., Donlon, C. J., Piskozub, J., Yelland, M. J., Ashton, I., Holding, T., Schuster, U., Girard-Ardhuin, F., Grouazel, A., Piolle, J. F., Warren, M., Wrobel-Niedzwiecka, I., Land, P. E., Torres, R., Prytherch, J., Moat, B., Hanafin, J., Ardhuin, F. and Paul, F.: Key Uncertainties in the Recent Air-Sea Flux of CO_2, Global Biogeochem. Cycles, 33(12), 1548–1563, doi:10.1029/2018GB006041, 2019.

Zeng, J., Nojiri, Y., Landschützer, P., Telszewski, M. and Nakaoka, S.: A global surface ocean fCO_2 climatology based on a feed-forward neural network, J. Atmos. Ocean. Technol., 31(8), 1838–1849, doi:10.1175/JTECH-D-13-00137.1, 2014.